Geological Magazine

www.cambridge.org/geo

Petrogenesis of Eocene Wangdui adakitic pluton in the western Gangdese belt, southern Tibet: implications for crustal thickening

Chang-da Wu[1], Yuan-chuan Zheng[2], Zeng-qian Hou[1], Pei-yan Xu[2], Lin-yuan Zhang[1], Yang Shen[2], Lu Wang[2] and Xin Li[2]

[1]Institute of Geology, Chinese Academy of Geological Sciences, Beijing 100037, People's Republic of China and [2]State Key Laboratory of Geological Processes and Mineral Resources, and School of Earth Sciences and Resources, China University of Geosciences, Beijing 100083, People's Republic of China

Original Article

Cite this article: Wu C-d, Zheng Y-c, Hou Z-q, Xu P-y, Zhang L-y, Shen Y, Wang L, and Li X (2022) Petrogenesis of Eocene Wangdui adakitic pluton in the western Gangdese belt, southern Tibet: implications for crustal thickening. *Geological Magazine* **159**: 1335–1354. https://doi.org/10.1017/S0016756822000206

Received: 7 July 2021
Revised: 15 January 2022
Accepted: 2 March 2022
First published online: 11 May 2022

Keywords:
crustal thickening; Eocene adakitic rocks; tectonic shortening; western Gangdese belt; Himalayan–Tibetan orogen

Author for correspondence:
Yuan-chuan Zheng,
Email: zhengyuanchuan@gmail.com

Abstract

Lower-crust-derived adakitic rocks in the Gangdese belt provide important constraints on the timing of Tibetan crustal thickening and on the relative contributions of magmatic and tectonic processes. Here we present geochronological and geochemical data for the Wangdui porphyritic monzogranites in the western Gangdese belt. Zircon U–Pb dating yields emplacement ages of 46–44 Ma. All samples have high Sr (321–599 ppm), low Yb (0.76–1.33 ppm) and Y (10.6–18.3 ppm) contents, with high La/Yb (51.1–72.3) and Sr/Y (21.0–51.4) ratios, indicating adakitic affinities. The low MgO (0.97–1.76 wt %), Cr (7.49–53.6 ppm) and Ni (4.75–29.1 ppm) contents, as well as high $^{87}Sr/^{86}Sr_{(i)}$ (0.7143–0.7145), low $\epsilon_{Nd}(t)$ (−10.4 to −9.8) and zircon $\epsilon_{Hf}(t)$ (−17.7 to 0.4) values, suggest that the Wangdui pluton most likely originated from partial melting of the thickened ancient lower crust. In combination with previously published data, despite the east–west-trending heterogeneity of crustal composition in the Gangdese belt, the La/Yb ratios of magmatic rocks reveal that both western and eastern segments experienced remarkable crustal thickening in the Eocene. However, in contrast to the thickened juvenile lower crust in the eastern segment formed by the underplating of mantle-derived magmas, tectonic shortening plays a more crucial role in thickening of the ancient basement in western Gangdese. In fact, such Eocene-thickened ancient lower-crust-derived adakitic rocks are widely distributed in the central Himalayan–Tibetan orogen. This, together with the extensive development of fold–thrust belts, suggests that tectonic shortening might be the main mechanism accounting for the crustal thickening associated with the India–Asia collision.

1. Introduction

The Himalayan–Tibetan orogen is the largest and highest continental collisional orogenic belt on Earth (Yin & Harrison, 2000), with the thickest continental crust (60–80 km) (Zhao *et al.* 2001; Kind *et al.* 2002). It has a profound influence on Asian monsoon development and global climate change (Harris, 2006; Dupont-Nivet *et al.* 2007). The timing of crustal thickening and plateau uplift, however, is still controversial, with estimates ranging from the Late Cretaceous to the Miocene (e.g. Volkmer *et al.* 2007; Chung *et al.* 2009; Ji *et al.* 2012*a*; Li *et al.* 2015; Ding *et al.* 2017; Zhu *et al.* 2017). Additionally, two main thickening mechanisms, namely tectonic shortening and magmatic underplating, have been proposed, but their relative contributions remain debated (e.g. Kapp *et al.* 2007; Mo *et al.* 2007; Volkmer *et al.* 2007; Ji *et al.* 2012*a*; Wang *et al.* 2014; Li *et al.* 2015; Zhu *et al.* 2017; Zhou *et al.* 2018).

Adakites, characterized by high La/Yb and Sr/Y ratios, were originally defined as the products of partial melting of young subducted oceanic slab (Defant & Drummond 1990). However, subsequent researches proposed that adakitic rocks can also be generated both in magmatic arcs and collisional orogens where the crust is thickened (Atherton & Petford 1993; Chung *et al.* 2003; Hou *et al.* 2004). Since the La/Yb and Sr/Y ratios of young intermediate-felsic rocks correlate well with the modern crustal thickness at regional to global scales, they are widely used to quantify crustal thickness changes over geological time (Chapman *et al.* 2015; Chiaradia 2015; Hu *et al.* 2017).

The Gangdese belt is located in the southern part of the Himalayan–Tibetan orogen. As the convergent zone of Indian and Asian plates, it is an ideal place to study the crustal thickening process related to continental collision. The La/Yb ratios of magmatic rocks suggest that the Gangdese belt experienced significant crustal thickening in the Eocene, which is generally attributed to the underplating of juvenile mantle-derived magmas (Mo *et al.* 2007; Guan *et al.* 2012; Ji *et al.* 2012*a*; Zhu *et al.* 2017; Zhou *et al.* 2018). However, previous studies have mostly focused on the magmatic records in the eastern Gangdese belt (east of 87° E), but rarely on the western segment (west of 87° E). Zircon Hf isotope mapping revealed a disparity in crustal composition

CAMBRIDGE UNIVERSITY PRESS

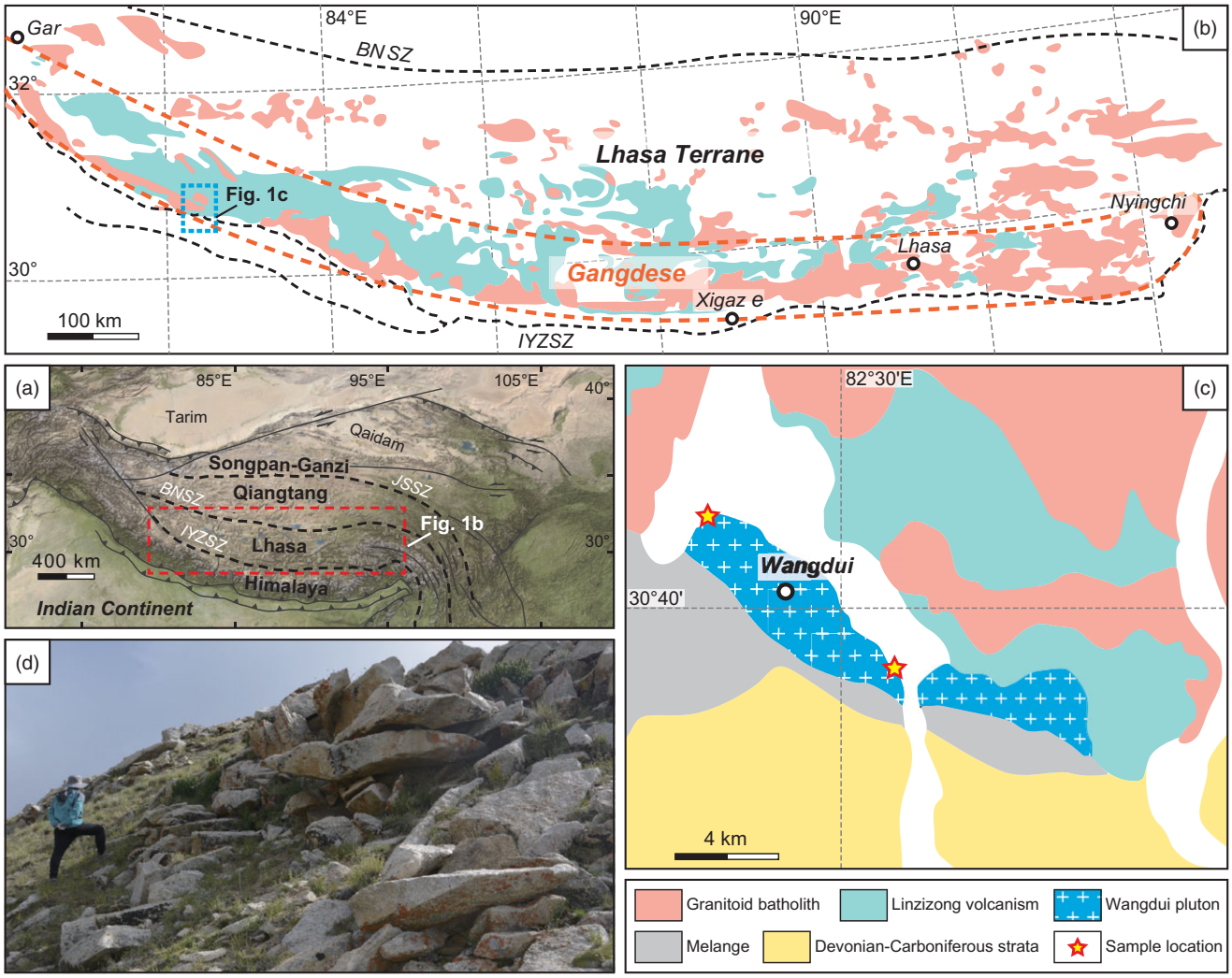

Fig. 1. (Colour online) (a) Tectonic framework of the Tibetan Plateau (modified from Li *et al.* 2015; the topographic base is from https://www.gebco.net). (b) Simplified geological map of Lhasa terrane, showing the location of the Gangdese belt (modified from Zheng *et al.* 2019). (c) Geological sketch map of the Wangdui pluton at the southern margin of the Lhasa terrane. (d) Field photograph of the Wangdui pluton. Abbreviations: BNSZ = Bangong–Nujiang suture zones; IYZSZ = Indus–Yarlung Zangbo suture zones; JSSZ = Jinsha suture zones.

between the eastern and western segments (Hou *et al.* 2015a), which implies that the two regions underwent diverse tectonic–magmatic evolutionary histories. Therefore, it is necessary to carry out a further investigation on the timing and mechanism of crustal thickening of the western Gangdese belt.

In this study, we present whole-rock elemental and Sr–Nd isotopic data, zircon U–Pb ages and Hf isotopic data for the Eocene Wangdui adakitic pluton in the western Gangdese belt. These, combined with previously published data, provide new constraints on the petrogenesis and source nature of Eocene adakitic rocks in the Gangdese belt. Ultimately, these data are conducive to gaining a better understanding of the crustal thickening process associated with the India–Asia continental collision.

2. Geological background and sample descriptions

The Tibetan Plateau is composed of four east–west-trending terranes: from north to south, they are Songpan–Ganzi, Qiangtang, Lhasa and Himalaya (Fig. 1a). These terranes are separated by the Jinsha, Bangong–Nujiang and Indus–Yarlung Zangbo suture zones, respectively, all of which represent the remnants of the Tethyan ocean (Yin & Harrison 2000). The Lhasa terrane, the southernmost tectonic unit of the Asian continent, was detached from Gondwana prior to the Triassic and then drifted northward across the Tethyan ocean until its collision with the Qiangtang terrane in the Early Cretaceous (Yin & Harrison 2000; Zhu *et al.* 2011; Wang *et al.* 2016).

The Gangdese belt is a huge tectonic–magmatic unit, which extends nearly east–west for more than 2000 km at the southern margin of the Lhasa terrane (Fig. 1b). Attributed to the subduction of Neo-Tethyan oceanic slab during the Triassic–Cretaceous and the subsequent continental collision between the Indian and Asian plates since *c.* 55–50 Ma, extensive Mesozoic–Cenozoic magmatism developed along the Gangdese belt, manifested as widespread volcanic rocks and the voluminous Gangdese batholith (Ji *et al.* 2009; Zhu *et al.* 2011, 2015, 2018; Hou *et al.* 2015*a*; Wang *et al.* 2016). The volcanic rocks are dominated by the Paleocene–Eocene Linzizong volcanic succession, with minor

https://doi.org/10.1017/S0016756822000206 Published online by Cambridge University Press

Triassic–Cretaceous volcano-sedimentary rocks and Oligocene–Miocene potassic–ultrapotassic volcanic rocks (e.g. Mo *et al.* 2008; Zhao *et al.* 2009; Kang *et al.* 2014; Wang *et al.* 2016; Wei *et al.* 2017). The Gangdese batholith was developed between the Triassic and Miocene (*c.* 210–10 Ma), with four activity peaks at 205–152 Ma, 109–80 Ma, 65–41 Ma and 33–13 Ma (e.g. Ji *et al.* 2009; Hou *et al.* 2015*a*; Zhu *et al.* 2018). The Mesozoic pre-collisional volcanic rocks and intrusions are mainly located in the eastern part of the Gangdese belt (e.g. Zheng *et al.* 2014; Xu *et al.* 2015; Wang *et al.* 2016; Wei *et al.* 2017; Wu *et al.* 2018), while the Cenozoic syn- to post-collisional magmatism is widely distributed along the entire belt extending from Nyingchi in the east to Gar in the west (e.g. Mo *et al.* 2008; Zhao *et al.* 2009; Hou *et al.* 2013; Q Wang *et al.* 2015; R Wang *et al.* 2015; Zheng *et al.* 2020).

The Wangdui pluton is located in the western part of the Gangdese batholith (*c.* 85 km east of Hor) and intruded into the Linzizong Formation (Fig. 1c, d). This pluton consists of medium- to coarse-grained monzogranites, which show porphyritic textures and contain megacrysts of plagioclase and K-feldspar. Mafic enclaves associated with pluton were not observed during the field studies. The minerals in the porphyritic monzogranites include K-feldspar (30–35 %), plagioclase (25–30 %), quartz (15–20 %), biotite (10–15 %), amphibole (*c.* 5 %) and minor accessory phases (zircon, apatite, titanite and magnetite) (Fig. 2). K-feldspar generally is subhedral, with locally developed cross-hatched twinning. Plagioclase commonly exhibits oscillatory zoning and Carlsbad-albite compound twinning. Sub- to anhedral biotite shows strong pleochroism and occasionally appears as mineral aggregates. Amphibole is dark green to brown in colour and prismatic in shape.

3. Analytical methods

The analytical methods are presented in Supplementary Text S1 (available online at https://doi.org/10.1017/S0016756822000206), and more detailed descriptions can be found in Andersen (2002), Ludwig (2003), Griffin *et al.* (2008) and Song *et al.* (2010) for U–Pb dating; in Blichert-Toft & Albarède (1997), Söderlund *et al.* (2004) and Wu *et al.* (2006) for zircon Hf isotopes; and in Chen *et al.* (2002) and Gou *et al.* (2012) for whole-rock geochemical analyses.

4. Results

4.a. Zircon U–Pb ages and Hf isotopes

Zircons from three porphyritic monzogranite samples (MYM15-1-1, MYM15-2-1, MYM15-2-7) were selected for U–Pb dating and Hf isotopic analyses. All the results of zircon U–Pb dating are provided in Table S1 (in the Supplementary Material available online at https://doi.org/10.1017/S0016756822000206) and are presented in concordia diagrams with 1σ errors in Fig. 3. The zircon Hf isotopic data and detailed calculation formulas are listed in Table 1.

The zircons from studied samples are mostly euhedral to subhedral, with crystal lengths of *c.* 80–350 μm, exhibiting oscillatory or planar zoning in cathodoluminescence (CL) images (Fig. 3). In addition, they have variable contents of Th (148–2377 ppm) and U (205–2028 ppm), with Th/U varying from 0.19 to 1.84. These features indicate that the analysed zircons are all of magmatic origin (Hoskin & Schaltegger, 2003). Thus, the measured zircon U–Pb ages represent the timing of zircon crystallization and thus the emplacement age of the host granitoids. Eighteen analyses of zircons from sample MYM15-1-1 yield $^{206}Pb/^{238}U$ ages ranging from 47.3 to 42.0 Ma, with a weighted mean $^{206}Pb/^{238}U$ age of 44.01 ± 0.67 Ma (MSWD = 0.88). Zircons from sample MYM15-2-1 yield $^{206}Pb/^{238}U$ ages ranging from 47.2 to 42.8 Ma for 16 analyses, which have a weighted mean $^{206}Pb/^{238}U$ age of 44.77 ± 0.63 Ma (MSWD = 0.94). The analyses of 16 zircons from sample MYM15-2-7 yield $^{206}Pb/^{238}U$ ages ranging from 49.0 to 43.4 Ma, with a weighted mean $^{206}Pb/^{238}U$ age of 46.00 ± 0.70 Ma (MSWD = 1.60).

A total of 45 zircons from three samples were analysed for $^{176}Hf/^{177}Hf$ isotopic ratios. Except for one zircon grain yielding a positive zircon $\epsilon_{Hf}(t)$ value (+0.4), the remaining 15 analyses from sample MYM15-1-1 yield $^{176}Hf/^{177}Hf$ ratios of 0.282350 to 0.282420 and $\epsilon_{Hf}(t)$ values of −14.0 to −11.5, with model ages calculated relative to the depleted mantle (T_{DM}(Hf)) ranging from 1.26 to 1.16 Ga and the crustal model ages (T_{DM}^{C}(Hf)) ranging from 2.01 to 1.85 Ga. Fourteen Hf analyses from sample MYM15-2-1 have $^{176}Hf/^{177}Hf$ ratios of 0.282370 to 0.282515, with negative $\epsilon_{Hf}(t)$ values ranging from −13.2 to −8.1. Their T_{DM}(Hf) ages and T_{DM}^{C}(Hf) ages range from 1.22 to 1.04 Ga and 1.96 to 1.64 Ga, respectively. Fifteen analyses of zircons from sample MYM15-2-7 show $^{176}Hf/^{177}Hf$ ratios ranging from 0.282244 to 0.282509, corresponding to $\epsilon_{Hf}(t)$ values of −17.7 to −8.3. They have T_{DM}(Hf) ages of 1.43 to 1.07 Ga and T_{DM}^{C}(Hf) ages of 2.24 to 1.65 Ga.

4.b. Whole-rock geochemistry

Whole-rock elemental and isotopic data are presented in Table 2. The Wangdui porphyritic monzogranites exhibit relatively limited variation in elemental composition (Figs 4–7). They belong to high-K calc-alkaline to shoshonitic series, with high SiO_2 contents of 66.52 to 70.98 wt % and K_2O contents of 3.72 to 5.02 wt % (Fig. 4a). The aluminium saturation index (A/CNK = Al_2O_3/(CaO + Na_2O + K_2O), molar ratios) values range from 0.90 to 1.00, showing a metaluminous feature (Fig. 4b). In particular, they are characterized by low MgO contents of 0.97 to 1.76 wt % and Mg# values of 38 to 48, with low compatible elements contents (e.g. Cr, 7.49–53.6 ppm; Ni, 4.75–29.1 ppm). In the chondrite-normalized rare earth element (REE) patterns, the porphyritic monzogranites show negative Eu anomalies (Eu/Eu* = 0.52–0.66) and fractionated REE patterns with enrichment of light REEs (LREEs) (Fig. 5a). The high La/Yb ratios of 51.1 to 72.3, low heavy REEs (HREEs) contents (e.g. Yb, 0.76–1.33 ppm) and Y contents of 10.6 to 18.3 ppm, together with high Sr contents of 321 to 599 ppm and Sr/Y ratios of 21.0 to 51.4, indicate that the samples have geochemical affinities with adakites (Fig. 4c, d). In addition, these samples show enrichments in large-ion lithophile elements (LILEs; e.g. Rb, K and Pb) and depletions in high-field-strength elements (HFSEs; e.g. Nb, Ta and Ti) in the primitive-mantle-normalized incompatible element patterns (Fig. 5b).

Six samples of Wangdui porphyritic monzogranites were analysed for whole-rock Sr–Nd isotopes. The initial isotopic ratios were calculated based on the measured zircon U–Pb ages. All these samples show homogeneous Sr–Nd isotopic features, with high $^{87}Sr/^{86}Sr_{(i)}$ ratios of 0.7143 to 0.7145 and low negative $\epsilon_{Nd}(t)$ values of −10.4 to −9.8. Their T_{DM}(Nd) and T_{DM2}(Nd) ages are 1.86–1.47 Ga and 1.73–1.60 Ga, respectively.

5. Discussion

5.a. Origin of the Wangdui porphyritic monzogranites

The Wangdui porphyritic monzogranites share geochemical affinities with adakites, characterized by high Sr contents, low HREEs

https://doi.org/10.1017/S0016756822000206 Published online by Cambridge University Press

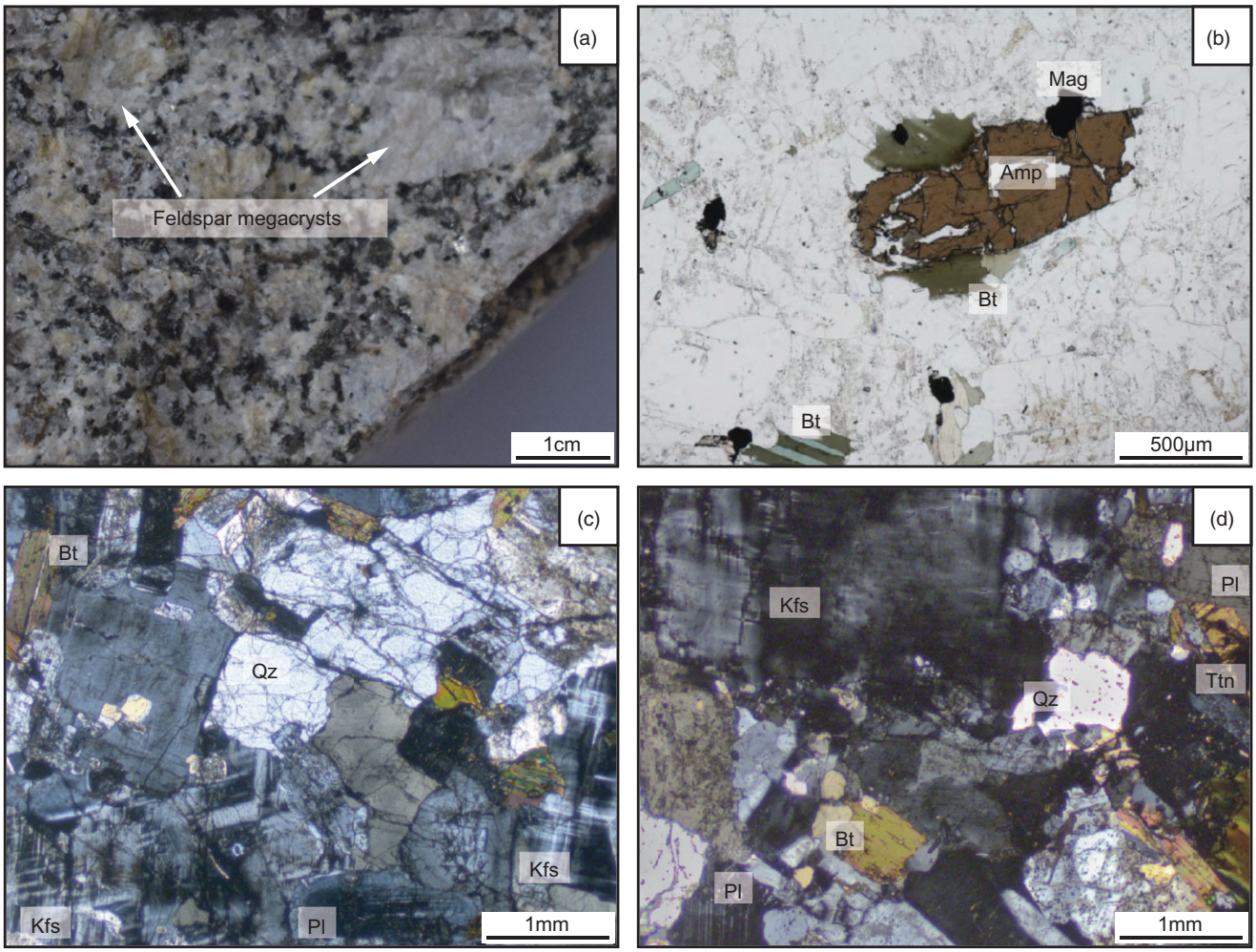

Fig. 2. (Colour online) (a) Hand specimen photo, and (b–d) photomicrographs of the Wangdui porphyritic monzogranites, southern Tibet. Abbreviations: Amp = amphibole; Bt = biotite; Kfs = K-feldspar; Mag = magnetite; Pl = plagioclase; Qz = quartz; Ttn = titanite.

and Y contents, and high La/Yb and Sr/Y ratios (Fig. 4c, d). In the past three decades, a variety of petrogenetic models for adakites (or adakitic rocks) have been proposed: (1) partial melting of subducted oceanic crust (Defant & Drummond 1990; Rapp *et al.* 1999; Zhu *et al.* 2009; Wu *et al.* 2018); (2) partial melting of subducted continental crust (Wang *et al.* 2008); (3) partial melting of delaminated lower continental crust (Xu *et al.* 2002; Wang *et al.* 2006); (4) partial melting of thickened lower crust (Atherton & Petford 1993; Chung *et al.* 2003; Hou *et al.* 2004, 2013; Zheng *et al.* 2012*a*, *b*); (5) crustal assimilation and fractional crystallization process of parental mafic magmas (Castillo *et al.* 1999; Macpherson *et al.* 2006); and (6) magma mixing between felsic and mafic magmas (Guo *et al.* 2007*a*; Streck *et al.* 2007). In this study, the following lines of evidence indicate that the Wangdui porphyritic monzogranites were most likely generated by partial melting of the thickened lower crust.

Adakitic rocks formed by fractional crystallization of parental mafic magmas typically show wide and continuous variations in geochemical compositions, and require the abundant presence of coeval mafic rocks (Castillo *et al.* 1999; Macpherson *et al.* 2006). However, the Wangdui pluton is exclusively felsic, with limited major element variations and uniform trace element patterns (Figs 5, 6a–c). Although some small volumes of coeval mantle-derived mafic magmas have been discovered in the western Gangdese belt (Dong *et al.* 2011; Q Wang *et al.* 2015; R Wang *et al.* 2015; Yu, 2015; Xia *et al.* 2020), they are more than 60 km away from the Wangdui and have significantly more depleted Sr–Nd–Hf isotopic compositions (Fig. 8a, b). Thus, the possibility that coeval mantle-derived mafic rocks were the parental magmas of the Wangdui pluton can be ruled out. In addition, a crucial geochemical feature of the fractional crystallization model (including high-pressure garnet fractionation and low-pressure amphibole fractionation) is that Sr/Y and La/Yb ratios should increase with increasing SiO_2 contents (Castillo *et al.* 1999; Macpherson *et al.* 2006), but Wangdui adakitic rocks do not display such evolutionary trends (Fig. 6d, e). Moreover, as shown in Figure 9, the positive correlation between Zr/Sm ratios and Zr contents is inconsistent with the fractional crystallization trend. Collectively, it is unlikely that the Wangdui adakitic rocks were generated by fractional crystallization of parental mafic magmas.

In general, adakitic rocks resulting from magma mixing between felsic and mafic magmas are andesitic in composition (Guo *et al.* 2007*a*; Streck *et al.* 2007), which is not the case for Wangdui porphyritic monzogranites. Additionally, mafic–felsic magma mixing would produce linear trends in element–element binary diagrams (Keller *et al.* 2015). However, the Wangdui adakitic rocks and the coeval mafic rocks in western Gangdese do not

https://doi.org/10.1017/S0016756822000206 Published online by Cambridge University Press

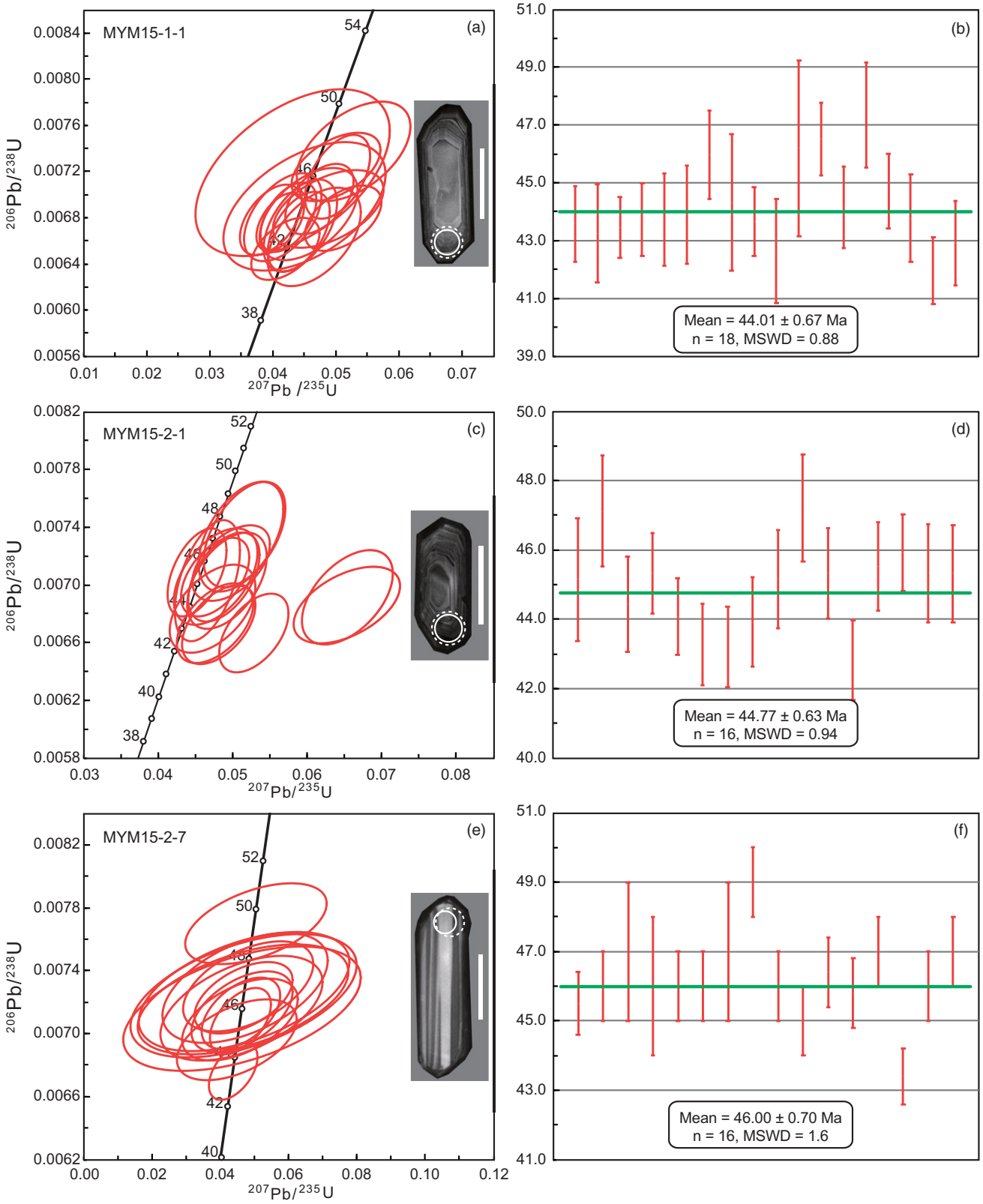

Fig. 3. (Colour online) CL images for representative zircon grains and U–Pb concordia diagrams for the Wangdui pluton, southern Tibet. Solid and dashed circles indicate the locations of laser ablation interactively coupled plasma mass spectrometry (LA-ICP-MS) U–Pb dating analyses and multi-collector LA-MC-ICP-MS Hf isotopic analyses, respectively. The scale bar length in the CL image is 100 μm.

https://doi.org/10.1017/S0016756822000206 Published online by Cambridge University Press

Table 1. Zircon Hf isotopic data for the Wangdui pluton, southern Tibet

Spot	Age (Ma)	$^{176}Yb/^{177}Hf$	$^{176}Lu/^{177}Hf$	$^{176}Hf/^{177}Hf$	2σ	$^{176}Hf/^{177}Hf_i$	$\epsilon_{Hf}(0)$	$\epsilon_{Hf}(t)$	T_{DM}(Hf) (Ma)	T_{DM}^{C}(Hf) (Ma)	$f_{Lu/Hf}$
MYM15-1-1, 44.01 ± 0.67 Ma, 16 spots, $\epsilon Hf(t) = -13.98$ to 0.41											
MYM1511–1	43.6	0.012600	0.000317	0.282389	0.000020	0.282388	−13.56	−12.61	1198	1922	−0.99
MYM1511–2	43.2	0.028384	0.000704	0.282351	0.000020	0.282350	−14.90	−13.98	1263	2008	−0.98
MYM1511–4	43.5	0.015071	0.000430	0.282420	0.000016	0.282420	−12.44	−11.50	1158	1852	−0.99
MYM1511–5	43.7	0.021156	0.000532	0.282391	0.000018	0.282391	−13.47	−12.53	1201	1917	−0.98
MYM1511–6	43.7	0.017673	0.000493	0.282396	0.000020	0.282395	−13.31	−12.36	1194	1907	−0.99
MYM1511–7	43.9	0.035779	0.000942	0.282757	0.000023	0.282756	−0.53	0.41	700	1095	−0.97
MYM1511–8	46.0	0.018130	0.000433	0.282390	0.000018	0.282390	−13.51	−12.52	1200	1918	−0.99
MYM1511–9	44.3	0.016021	0.000497	0.282410	0.000018	0.282409	−12.81	−11.86	1175	1875	−0.99
MYM1511–10	43.7	0.016007	0.000388	0.282385	0.000019	0.282385	−13.68	−12.73	1205	1930	−0.99
MYM1511–14	46.5	0.015851	0.000413	0.282381	0.000020	0.282380	−13.84	−12.84	1212	1939	−0.99
MYM1511–15	44.2	0.025867	0.000635	0.282388	0.000018	0.282387	−13.60	−12.65	1209	1925	−0.98
MYM1511–16	47.3	0.016195	0.000421	0.282386	0.000018	0.282386	−13.65	−12.63	1205	1926	−0.99
MYM1511–17	44.7	0.017022	0.000437	0.282350	0.000020	0.282350	−14.91	−13.94	1254	2007	−0.99
MYM1511–18	43.8	0.017126	0.000445	0.282352	0.000018	0.282352	−14.84	−13.90	1252	2004	−0.99
MYM1511–19	42.0	0.011764	0.000327	0.282365	0.000018	0.282364	−14.41	−13.50	1231	1977	−0.99
MYM1511–20	42.9	0.020152	0.000494	0.282409	0.000017	0.282409	−12.82	−11.90	1175	1877	−0.99
MYM15-2-1, 44.77 ± 0.63 Ma, 14 spots, $\epsilon Hf(t) = -13.20$ to −8.11											
MYM1521–1	45.1	0.012530	0.000307	0.282439	0.000017	0.282439	−11.77	−10.79	1128	1808	−0.99
MYM1521–4	47.1	0.018128	0.000440	0.282436	0.000019	0.282436	−11.87	−10.85	1136	1813	−0.99
MYM1521–5	44.4	0.018557	0.000444	0.282438	0.000018	0.282438	−11.80	−10.84	1133	1811	−0.99
MYM1521–7	45.3	0.017147	0.000417	0.282443	0.000018	0.282443	−11.62	−10.64	1126	1799	−0.99
MYM1521–9	43.3	0.025584	0.000639	0.282425	0.000021	0.282424	−12.28	−11.35	1158	1842	−0.98
MYM1521–10	43.2	0.020899	0.000511	0.282499	0.000020	0.282498	−9.66	−8.73	1052	1676	−0.98
MYM1521–11	43.9	0.013410	0.000346	0.282497	0.000020	0.282496	−9.74	−8.79	1050	1680	−0.99
MYM1521–12	45.2	0.015771	0.000389	0.282508	0.000019	0.282507	−9.35	−8.37	1036	1655	−0.99
MYM1521–13	47.2	0.014386	0.000317	0.282370	0.000018	0.282370	−14.22	−13.20	1224	1962	−0.99
MYM1521–15	45.3	0.016778	0.000420	0.282444	0.000020	0.282443	−11.61	−10.63	1125	1798	−0.99
MYM1521–17	45.5	0.021570	0.000504	0.282505	0.000017	0.282505	−9.44	−8.46	1043	1660	−0.98
MYM1521–18	45.9	0.034858	0.000848	0.282515	0.000020	0.282514	−9.09	−8.11	1038	1638	−0.97
MYM1521–19	45.3	0.021936	0.000533	0.282461	0.000018	0.282461	−10.99	−10.01	1104	1759	−0.98
MYM1521–20	45.3	0.009445	0.000235	0.282450	0.000019	0.282450	−11.37	−10.38	1110	1783	−0.99
MYM15-2-7, 46.00 ± 0.70 Ma, 15 spots, $\epsilon Hf(t) = -17.69$ to −8.32											
MYM15-2-7-01	45.5	0.034111	0.001028	0.282394	0.000019	0.282393	−13.35	−12.39	1212	1909	−0.97
MYM15-2-7-02	46.0	0.048662	0.001538	0.282509	0.000017	0.282508	−9.28	−8.32	1065	1652	−0.95
MYM15-2-7-03	47.0	0.034069	0.001135	0.282398	0.000018	0.282397	−13.24	−12.25	1211	1901	−0.97
MYM15-2-7-04	46.0	0.024745	0.000782	0.282354	0.000018	0.282353	−14.78	−13.80	1261	1999	−0.98
MYM15-2-7-05	46.0	0.018695	0.000601	0.282296	0.000017	0.282296	−16.82	−15.83	1335	2127	−0.98
MYM15-2-7-07	47.0	0.019165	0.000619	0.282358	0.000016	0.282357	−14.65	−13.64	1250	1990	−0.98
MYM15-2-7-09	49.0	0.024907	0.000815	0.282338	0.000018	0.282338	−15.34	−14.29	1284	2032	−0.98
MYM15-2-7-12	46.0	0.023118	0.000732	0.282314	0.000017	0.282314	−16.18	−15.20	1314	2087	−0.98
MYM15-2-7-13	45.0	0.042899	0.001315	0.282256	0.000019	0.282254	−18.26	−17.32	1417	2220	−0.96

(*Continued*)

https://doi.org/10.1017/S0016756822000206 Published online by Cambridge University Press

Table 1. (*Continued*)

Spot	Age (Ma)	$^{176}Yb/^{177}Hf$	$^{176}Lu/^{177}Hf$	$^{176}Hf/^{177}Hf$	2σ	$^{176}Hf/^{177}Hf_i$	$\epsilon_{Hf}(0)$	$\epsilon_{Hf}(t)$	$T_{DM}(Hf)$ (Ma)	$T_{DM}^{C}(Hf)$ (Ma)	$f_{Lu/Hf}$
MYM15-2-7-14	46.4	0.028949	0.000966	0.282297	0.000019	0.282296	−16.80	−15.81	1346	2126	−0.97
MYM15-2-7-15	45.8	0.013863	0.000446	0.282320	0.000015	0.282320	−15.97	−14.98	1296	2074	−0.99
MYM15-2-7-16	47.0	0.007974	0.000288	0.282325	0.000012	0.282325	−15.81	−14.79	1285	2063	−0.99
MYM15-2-7-17	43.4	0.015253	0.000549	0.282345	0.000015	0.282344	−15.11	−14.17	1266	2021	−0.98
MYM15-2-7-19	46.0	0.036710	0.001177	0.282244	0.000018	0.282243	−18.66	−17.69	1428	2244	−0.96
MYM15-2-7-20	47.0	0.036868	0.001178	0.282442	0.000021	0.282441	−11.67	−10.68	1150	1802	−0.96

Notes: $\epsilon_{Hf}(t) = 10000 \times \{[(^{176}Hf/^{177}Hf)_S - (^{176}Lu/^{177}Hf)_S \times (e^{\lambda t} - 1)]/[(^{176}Hf/^{177}Hf)_{CHUR,0} - (^{176}Lu/^{177}Hf)_{CHUR} \times (e^{\lambda t} - 1)] - 1\}$.
$T_{DM}(Hf) = 1/\lambda \times \ln\{1 + [(^{176}Hf/^{177}Hf)_S - (^{176}Hf/^{177}Hf)_{DM}]/[(^{176}Lu/^{177}Hf)_S - (^{176}Lu/^{177}Hf)_{DM}]\}$.
$T_{DM}^{C}(Hf) = 1/\lambda \times \ln\{1 + [(^{176}Hf/^{177}Hf)_{S,\ t} - (^{176}Hf/^{177}Hf)_{DM,\ t}]/[(^{176}Lu/^{177}Hf)_C - (^{176}Lu/^{177}Hf)_{DM}]\} + t$.
$f_{Lu/Hf} = (^{176}Lu/^{177}Hf)_S/(^{176}Lu/^{177}Hf)_{CHUR} - 1$.
$(^{176}Lu/^{177}Hf)_{CHUR} = 0.0332$ and $(^{176}Hf/^{177}Hf)_{CHUR,0} = 0.282772$ (Blichert-Toft & Albarède, 1997); $(^{176}Lu/^{177}Hf)_{DM} = 0.0384$ and $(^{176}Hf/^{177}Hf)_{DM} = 0.28325$ (Griffin *et al.* 2000); $\lambda = 1.867 \times 10^{-11}$ year^{-1} (Söderlund *et al.* 2004); $(^{176}Lu/^{177}Hf)_C = 0.015$, t = crystallization age of zircon.

show linear correlations of Al_2O_3, Na_2O and P_2O_5 with SiO_2 (Fig. 6a–c). Besides, no mafic enclaves have been discovered in the Wangdui area during field investigations, which further implies that the effect of magma mixing was negligible.

Previous studies have shown that Neo-Tethyan ocean closure and India–Asia continental collision occurred at *c.* 55–50 Ma (van Hinsbergen *et al.* 2011; Zhu *et al.* 2015; Ding *et al.* 2016), so the Wangdui porphyritic monzogranites were formed in an intra-continental setting, which is inconsistent with the tectonic settings for partial melting of subducted oceanic crust. In the Gangdese belt, typical adakites derived from oceanic slab melting were mostly emplaced during the Mesozoic (e.g. Zhu *et al.* 2009; Zhang *et al.* 2010; Ma *et al.* 2013; Wu *et al.* 2018), and are characterized by high MgO, Cr, Ni contents and Mg# values (Fig. 7a–d). By contrast, Wangdui adakitic samples show low contents of MgO and compatible elements, as well as low Mg# values. In addition, oceanic slab-derived adakites are generally expected to have low K_2O/Na_2O (<0.71) and high CaO/Al_2O_3 (>0.2) ratios (e.g. Stern & Kilian 1996; Li *et al.* 2016). The high K_2O/Na_2O (1.09–1.64) and low CaO/Al_2O_3 (0.16–0.21) ratios of Wangdui pluton (Fig. 7e), therefore, also argue against an oceanic slab origin. This is further supported by isotopic evidence, wherein Wangdui adakitic rocks have low whole-rock $\epsilon_{Nd}(t)$ (−10.4 to −9.8) and zircon $\epsilon_{Hf}(t)$ (−17.7 to 0.4) values, distinct from the isotopic characteristics of oceanic crust. Consequently, the Wangdui porphyritic monzogranites were also unlikely to be generated by partial melting of subducted oceanic crust.

The presence of the Eocene mantle-derived gabbros in the western Gangdese batholith (Dong *et al.* 2011; Q Wang *et al.* 2015; Yu, 2015; Xia *et al.* 2020) indicates that the mantle beneath this region was well preserved rather than being squeezed out by subducted Indian plate. In this case, the ascending melts derived from subducted continental crust would inevitably react with the overlying mantle wedge, causing the increase in MgO and compatible elements contents (Fig. 7a–d) (Rapp *et al.* 1999; Wang *et al.* 2008). However, as mentioned above, this is in contrast to the geochemical compositions of Wangdui porphyritic monzogranites. Moreover, according to the deep seismic reflection studies, most of the Indian continental crust was scraped off to form the accretionary wedge by crustal-scale duplexing, and thus only a thin layer of Indian crust was underthrust beneath the Lhasa terrane (Nábělek *et al.* 2009; Gao *et al.* 2016). This also implies a low possibility of the subducted continental crust melting model.

Partial melting of delaminated lower continental crust commonly occurs in intra-continental extensional settings (Xu *et al.* 2002; Wang *et al.* 2006). However, the relatively high India–Asia convergence rate (*c.* 80–100 mm year^{-1}) during 51–45 Ma (van Hinsbergen *et al.* 2011), together with the development of east–west-trending thrust systems in the region (Hou & Cook, 2009; Li *et al.* 2015), indicates that the Wangdui pluton was emplaced in a compressional environment. Additionally, adakitic rocks derived from delaminated lower crust also typically have high MgO and compatible elements contents due to the interaction with the overlying mantle (Xu *et al.* 2002; Wang *et al.* 2006), which is not observed in Wangdui adakitic rocks. Besides, considering the relatively depleted isotopic compositions of coeval mantle-derived rocks (Fig. 8a, b), melt–mantle interaction would cause the increase in $\epsilon_{Nd}(t)$ and $\epsilon_{Hf}(t)$ values of the resulting adakitic magmas (Wang *et al.* 2006). In contrast, the Wangdui porphyritic monzogranites show highly enriched isotopic signatures, which are similar to those of the ancient Gangdese basement (see Section 5.b). Thus, the delaminated model is unsuitable for the formation of the Wangdui porphyritic monzogranites.

The only remaining candidate is the thickened lower crust, which could serve as the source region for the Wangdui adakitic rocks. This inference is supported by the observation that the low MgO and compatible elements contents of Wangdui samples are comparable to those of the previously reported Eocene–Miocene adakitic intrusions in the Gangdese belt (Fig. 7a–d), which have been interpreted as the products of partial melting of the thickened lower crust (e.g. Hou *et al.* 2004, 2013; Guan *et al.* 2012; Zheng *et al.* 2012*a*, *b*, 2020; Ma *et al.* 2014). In fact, as well as in the Gangdese belt, similar low MgO, Cr and Ni signatures are also present in Cenozoic thickened-crust-derived adakitic rocks in other collisional orogenic systems, such as Turkey and Iran (e.g. Topuz *et al.* 2005; Shafiei *et al.* 2009; Karsli *et al.* 2011, 2019; Pang *et al.* 2016). Moreover, the Wangdui pluton has high K_2O and Th contents, with high K_2O/Na_2O and low CaO/Al_2O_3 ratios (Fig. 7e, f), further suggesting a continental crust affinity (Zhu *et al.* 2009; Chen *et al.* 2013; Karsli *et al.* 2019). Therefore, we suggest that the Wangdui porphyritic monzogranites were derived from partial melting of the thickened lower continental crust.

https://doi.org/10.1017/S0016756822000206 Published online by Cambridge University Press

Table 2. Whole-rock major, trace element and Sr–Nd isotopic data for the Wangdui pluton

Sample	MYM15-1-3	MYM15-1-4	MYM15-1-5	MYM15-1-6	MYM15-2-2	MYM15-2-4	MYM15-2-5	MYM15-2-6	MYM15-2-8	MYM15-2-10	MYM15-2-11	MYM15-2-12
Age (Ma)	44.01	44.01	44.01	44.01	44.77	44.77	44.77	44.77	46.00	46.00	46.00	46.00
Long. (° E)	82.54	82.54	82.54	82.54	82.44	82.44	82.44	82.44	82.44	82.44	82.44	82.44
Lat. (° N)	30.64	30.64	30.64	30.64	30.69	30.69	30.69	30.69	30.69	30.69	30.69	30.69
XRF: major element (wt %)												
SiO_2	69.90	69.68	70.12	70.98	67.73	67.85	68.65	66.52	70.23	70.26	67.61	69.33
TiO_2	0.52	0.52	0.61	0.52	0.51	0.51	0.50	0.60	0.52	0.49	0.71	0.61
Al_2O_3	14.04	14.01	13.43	13.31	14.39	14.31	13.94	14.45	13.85	14.05	14.62	14.18
TFe_2O_3	3.20	3.18	3.86	3.26	3.39	3.43	3.36	3.99	3.08	2.82	3.85	3.38
MnO	0.06	0.06	0.07	0.05	0.06	0.05	0.06	0.07	0.04	0.04	0.05	0.04
MgO	0.98	1.00	1.17	1.05	1.54	1.55	1.43	1.76	0.97	0.98	1.34	1.11
CaO	2.34	2.42	2.82	2.47	2.90	2.76	2.70	3.00	2.28	2.34	2.93	2.40
Na_2O	3.16	3.07	3.01	3.02	3.32	3.23	3.06	3.20	2.93	3.17	3.45	3.28
K_2O	4.55	4.80	3.72	4.12	4.86	4.88	5.02	4.92	4.55	4.38	3.75	4.13
P_2O_5	0.18	0.17	0.22	0.19	0.21	0.20	0.21	0.23	0.15	0.16	0.22	0.18
LOI	0.93	0.94	0.84	0.89	0.91	1.08	0.89	1.07	1.24	1.19	1.32	1.20
Total	99.85	99.86	99.87	99.87	99.82	99.85	99.82	99.80	99.84	99.87	99.85	99.83
A/NK	1.38	1.37	1.49	1.41	1.34	1.35	1.33	1.36	1.42	1.41	1.50	1.44
A/CNK	0.97	0.96	0.95	0.95	0.90	0.92	0.90	0.90	1.00	0.99	0.97	1.00
Mg#	38.06	38.69	37.73	39.09	47.61	47.42	46.08	46.83	38.73	40.92	41.09	39.59
ICP-MS: trace element (ppm)												
Li	49.5	65.6	69.0	60.3	52.1	48.3	55.8	63.0	52.9	51.4	59.5	52.6
Be	5.22	5.02	6.63	5.43	9.72	6.35	7.55	9.40	4.57	5.08	6.06	4.53
Sc	5.75	7.54	9.10	6.51	7.04	6.96	23.9	17.6	5.20	5.70	8.31	7.64
V	49.8	51.3	66.0	55.9	65.8	62.6	65.8	79.8	54.3	53.9	72.5	60.3
Cr	12.7	12.2	17.7	15.5	43.9	40.7	44.6	53.6	7.57	8.19	9.23	7.49
Co	6.10	6.59	8.26	6.88	8.98	9.20	9.49	11.7	6.31	6.17	8.26	7.01
Ni	8.97	9.28	12.0	10.4	23.9	22.4	29.1	27.7	5.63	5.27	6.45	4.75
Cu	7.12	9.36	11.8	9.04	9.74	7.87	7.97	6.89	32.9	21.8	19.8	19.6
Zn	21.6	22.2	35.7	30.2	32.7	19.3	29.3	29.9	21.4	45.6	29.3	17.9
Ga	19.6	20.4	23.2	21.0	22.1	20.5	21.5	23.6	20.3	21.0	23.4	21.0
Rb	245	291	277	266	341	271	333	358	318	331	311	311
Sr	321	389	381	362	575	449	553	599	399	410	386	373
Y	11.0	13.3	15.8	14.0	11.4	10.6	10.7	14.0	12.8	13.0	18.3	15.9
Zr	189	247	496	333	146	412	230	189	191	208	265	259
Nb	20.1	21.4	24.9	22.3	26.2	23.3	22.8	29.4	15.2	16.1	21.1	19.0
Mo	0.01	0.01	0.02	0.12	6.36	0.65	0.90	1.79	0.35	0.77	1.12	1.05
Cd	0.06	0.08	0.14	0.10	0.14	0.13	0.08	0.10	0.06	0.07	0.08	0.06
Sn	3.92	13.1	4.91	4.82	5.78	4.70	4.50	6.13	3.66	3.67	5.08	4.48
Cs	9.06	18.3	15.2	19.9	52.0	40.8	41.2	51.7	27.1	36.4	42.9	40.3
Ba	576	754	458	517	987	1025	979	1062	1017	1032	796	974
La	48.5	54.8	63.3	59.9	54.9	48.6	55.2	62.9	58.5	54.0	78.8	72.7
Ce	99.8	106	123	114	107	98.4	103	122	114	105	155	142

(*Continued*)

https://doi.org/10.1017/S0016756822000206 Published online by Cambridge University Press

Table 2. (*Continued*)

Sample	MYM15-1-3	MYM15-1-4	MYM15-1-5	MYM15-1-6	MYM15-2-2	MYM15-2-4	MYM15-2-5	MYM15-2-6	MYM15-2-8	MYM15-2-10	MYM15-2-11	MYM15-2-12
Pr	9.78	11.5	13.2	12.0	11.8	10.6	10.9	13.6	12.1	11.5	16.9	15.2
Nd	32.1	40.4	42.6	39.5	38.7	36.3	35.1	44.5	38.9	38.6	56.0	53.3
Sm	6.26	7.93	7.71	6.90	8.03	7.62	7.40	9.17	7.67	7.63	11.1	10.0
Eu	1.02	1.27	1.28	1.18	1.46	1.40	1.34	1.64	1.34	1.39	1.66	1.58
Gd	4.33	5.27	5.83	5.27	5.04	4.74	4.57	5.91	5.16	5.16	7.51	6.91
Tb	0.45	0.56	0.63	0.56	0.50	0.47	0.45	0.59	0.54	0.55	0.79	0.72
Dy	2.03	2.52	2.83	2.53	2.09	1.98	1.89	2.47	2.41	2.43	3.51	3.21
Ho	0.36	0.45	0.50	0.45	0.36	0.34	0.33	0.42	0.42	0.42	0.61	0.56
Er	0.94	1.18	1.33	1.20	0.90	0.88	0.87	1.09	1.10	1.10	1.58	1.45
Tm	0.13	0.17	0.19	0.17	0.12	0.12	0.12	0.15	0.15	0.15	0.22	0.20
Yb	0.85	1.07	1.22	1.08	0.81	0.80	0.76	0.94	0.96	0.93	1.33	1.22
Lu	0.12	0.15	0.18	0.16	0.11	0.12	0.11	0.13	0.13	0.13	0.18	0.17
Hf	5.64	7.24	13.6	9.38	4.64	11.7	6.92	5.93	5.27	5.87	7.68	7.45
Ta	1.61	1.92	2.15	1.99	2.42	2.07	2.35	2.86	1.15	1.35	2.01	1.96
Tl	1.13	1.36	1.24	1.28	1.65	1.61	1.60	1.66	1.63	1.75	1.67	1.74
Pb	39.9	46.9	38.1	41.0	51.4	56.6	58.7	51.9	44.6	49.3	45.5	52.2
Th	31.4	38.1	42.0	43.6	43.3	41.5	44.9	45.9	38.1	38.9	42.1	43.9
U	4.27	4.04	4.28	4.77	11.5	10.2	9.19	10.3	3.06	3.51	4.47	4.33
Sr/Y	29.3	29.2	24.1	25.9	50.3	42.2	51.4	42.9	31.3	31.6	21.0	23.4
La/Yb	57.2	51.1	52.1	55.3	68.1	60.7	72.3	66.7	61.2	58.0	59.4	59.4
Eu/Eu*	0.56	0.57	0.56	0.57	0.66	0.66	0.66	0.64	0.61	0.64	0.52	0.55
$^{87}Rb/^{86}Sr$	2.2082	2.1620		2.1298	1.7183		1.7454	1.7292				
$^{87}Sr/^{86}Sr$	0.715717	0.715812		0.715810	0.715610		0.715581	0.715615				
2σ	0.000010	0.000012		0.000012	0.000009		0.000012	0.000009				
$(^{87}Sr/^{86}Sr)_i$	0.714336	0.714461		0.714479	0.714536		0.714490	0.714534				
$^{147}Sm/^{144}Nd$	0.1178	0.1187		0.1057	0.1252		0.1275	0.1246				
$^{143}Nd/^{144}Nd$	0.512109	0.512108		0.512109	0.512086		0.512097	0.512091				
2σ	0.000009	0.000008		0.000009	0.000007		0.000007	0.000008				
$(^{143}Nd/^{144}Nd)_i$	0.512075	0.512074		0.512078	0.512050		0.512060	0.512055				
$\epsilon_{Nd}(t)$	−9.88	−9.89		−9.82	−10.36		−10.17	−10.27				
$f_{Sm/Nd}$	−0.40	−0.40		−0.46	−0.36		−0.35	−0.37				
T_{DM}(Nd) (Ma)	1654	1671		1470	1831		1861	1810				
T_{DM2}(Nd) (Ma)	1657	1662		1602	1727		1721	1717				

Notes: TFe_2O_3 = Total iron measured as Fe_2O_3.
LOI = loss on ignition.
A/NK = $Al_2O_3/(Na_2O + K_2O)$ (molar ratio).
A/CNK = $Al_2O_3/(CaO + Na_2O + K_2O)$ (molar ratio).
Mg# = $100 \times Mg^{2+}/(Mg^{2+} + Fe^{2+})$.
Eu/Eu* = $2 \times Eu_n/(Sm_n + Gd_n)$.
$(^{87}Sr/^{86}Sr)_i = (^{87}Sr/^{86}Sr)s - (^{87}Rb/^{86}Sr) \times (e^{\lambda T} - 1)$, $\lambda_{Rb\text{-}Sr} = 1.42 \times 10^{-11}$ year^{-1}, $^{87}Rb/^{86}Sr = (Rb/Sr) \times 2.8956$.
$\epsilon_{Nd}(t) = [(^{143}Nd/^{144}Nd)_i/(^{143}Nd/^{144}Nd)_{CHUR}(t) - 1] \times 10000$, $(^{143}Nd/^{144}Nd)_i = (^{143}Nd/^{144}Nd)_s - (^{147}Sm/^{144}Nd) \times (e^{\lambda T} - 1)$, $(^{143}Nd/^{144}Nd)_{CHUR}(t) = 0.512638 - 0.1967 \times (e^{\lambda T} - 1)$, $\lambda_{Sm\text{-}Nd} = 6.54 \times 10^{-12}$ year^{-1}, $^{147}Sm/^{144}Nd = (Sm/Nd) \times 0.60456$.
$T_{DM} = 1/\lambda_{Sm\text{–}Nd} \times \ln\{1 + [(^{143}Nd/^{144}Nd)_s - 0.51315)/((^{147}Sm/^{144}Nd)_s - 0.21357)]\}$.
T_{DM2} is the two-stage Nd depleted-mantle model age calculated using the same assumption formulation as Keto and Jacobsen (1987).

https://doi.org/10.1017/S0016756822000206 Published online by Cambridge University Press

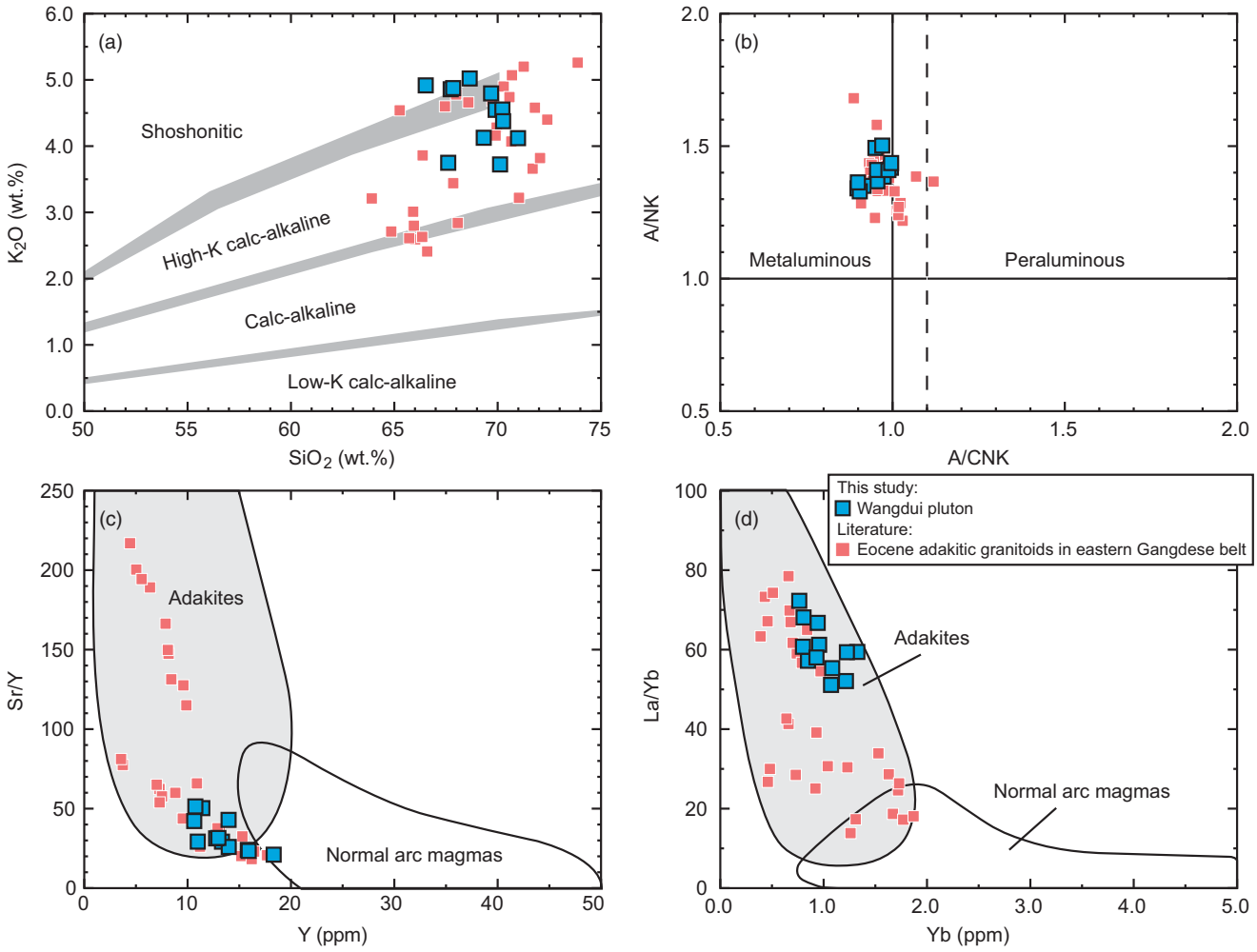

Fig. 4. (Colour online) (a) K_2O vs SiO_2 (Peccerillo & Taylor, 1976), (b) A/NK [$Al_2O_3/(Na_2O + K_2O)$] vs A/CNK [$Al_2O_3/(CaO + Na_2O + K_2O)$], (c) Sr/Y vs Y and (d) La/Yb vs Yb plots for the Wangdui pluton. The fields of adakites and normal arc magmas are from Defant & Drummond (1990) and Sun *et al.* (2012). Data for Eocene adakitic granitoids in the eastern Gangdese belt are from Guan *et al.* (2012), Ji *et al.* (2012a), Ma *et al.* (2014) and our unpublished data.

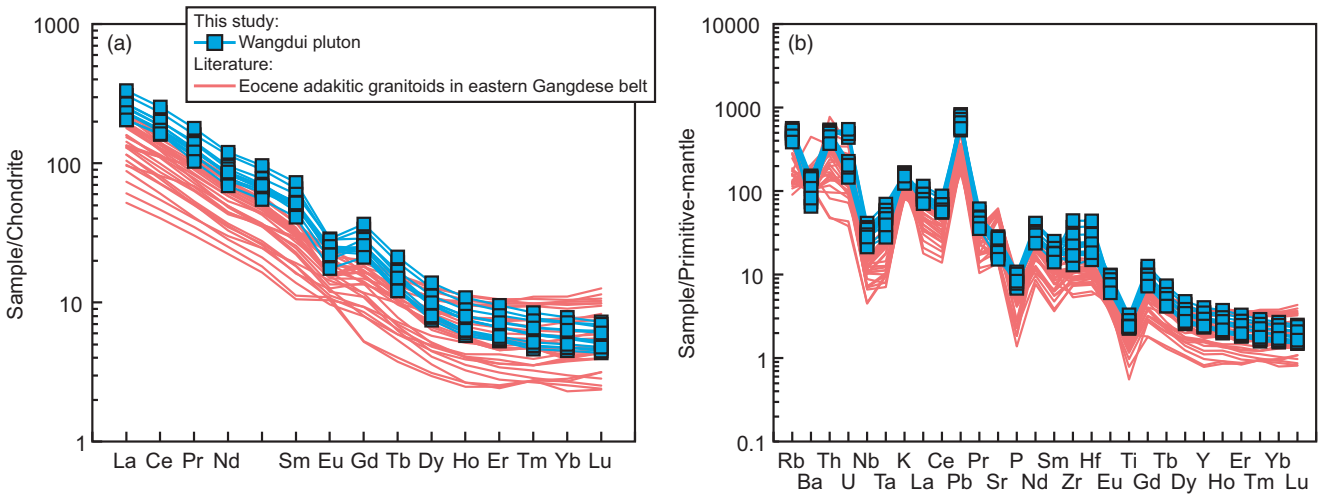

Fig. 5. (Colour online) (a) Chondrite-normalized REE patterns, and (b) primitive-mantle-normalized trace element patterns for the Wangdui pluton. Chondrite and primitive-mantle-normalizing values are from Sun & McDonough (1989). Data for Eocene adakitic granitoids in the eastern Gangdese belt are from the same source as Figure 4.

https://doi.org/10.1017/S0016756822000206 Published online by Cambridge University Press

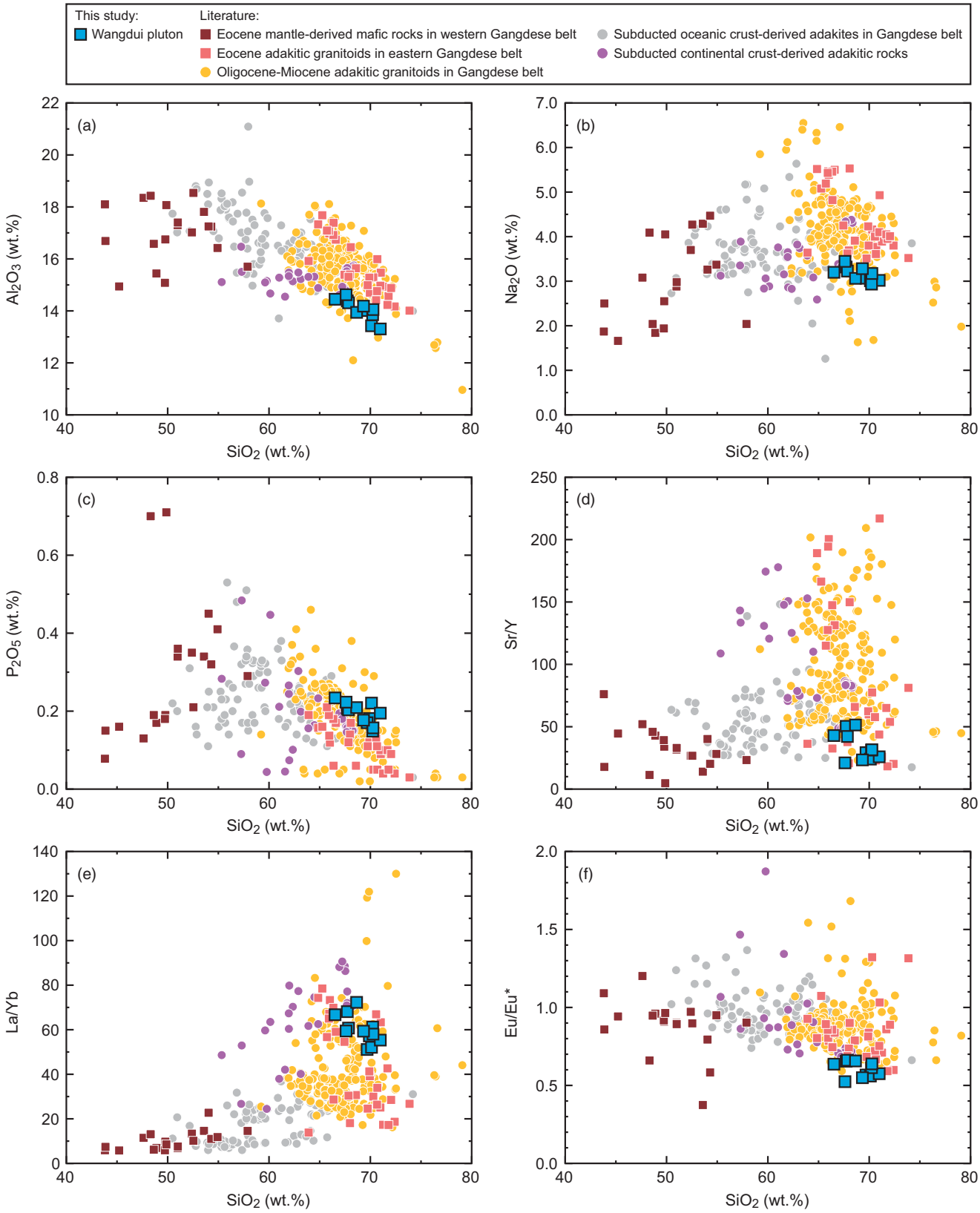

Fig. 6. (Colour online) (a) Al_2O_3, (b) Na_2O, (c) P_2O_5, (d) Sr/Y, (e) La/Yb and (f) Eu/Eu* [$2 \times Eu_n/(Sm_n + Gd_n)$] vs SiO_2 plots for the Wangdui pluton. Data for Eocene mantle-derived mafic rocks in the western Gangdese belt are from Dong *et al.* (2011), Zhu *et al.* (2011), R Wang *et al.* (2015), Yu (2015) and Xia *et al.* (2020). Data for Oligocene–Miocene adakitic granitoids in the Gangdese belt are from Hou *et al.* (2004, 2013), Guo *et al.* (2007*b*), Yang (2008), Chen *et al.* (2011), Zheng *et al.* (2012*a*, 2012*b*, 2020), Hu *et al.* (2015), Yu (2015), Zhao *et al.* (2015), Li *et al.* (2017) and Sun *et al.* (2018). Data for subducted oceanic crust-derived adakites in the Gangdese belt are from Zhu *et al.* (2009), Zhang *et al.* (2010), Jiang *et al.* (2012, 2014), Ma *et al.* (2013), Zheng *et al.* (2014), L Chen *et al.* (2015), YH Chen et al. (2015) and Wu *et al.* (2018). Data for subducted continental-crust-derived adakitic rocks are from Wang *et al.* (2008). Data for Eocene adakitic granitoids in the eastern Gangdese belt are from the same source as Figure 4.

https://doi.org/10.1017/S0016756822000206 Published online by Cambridge University Press

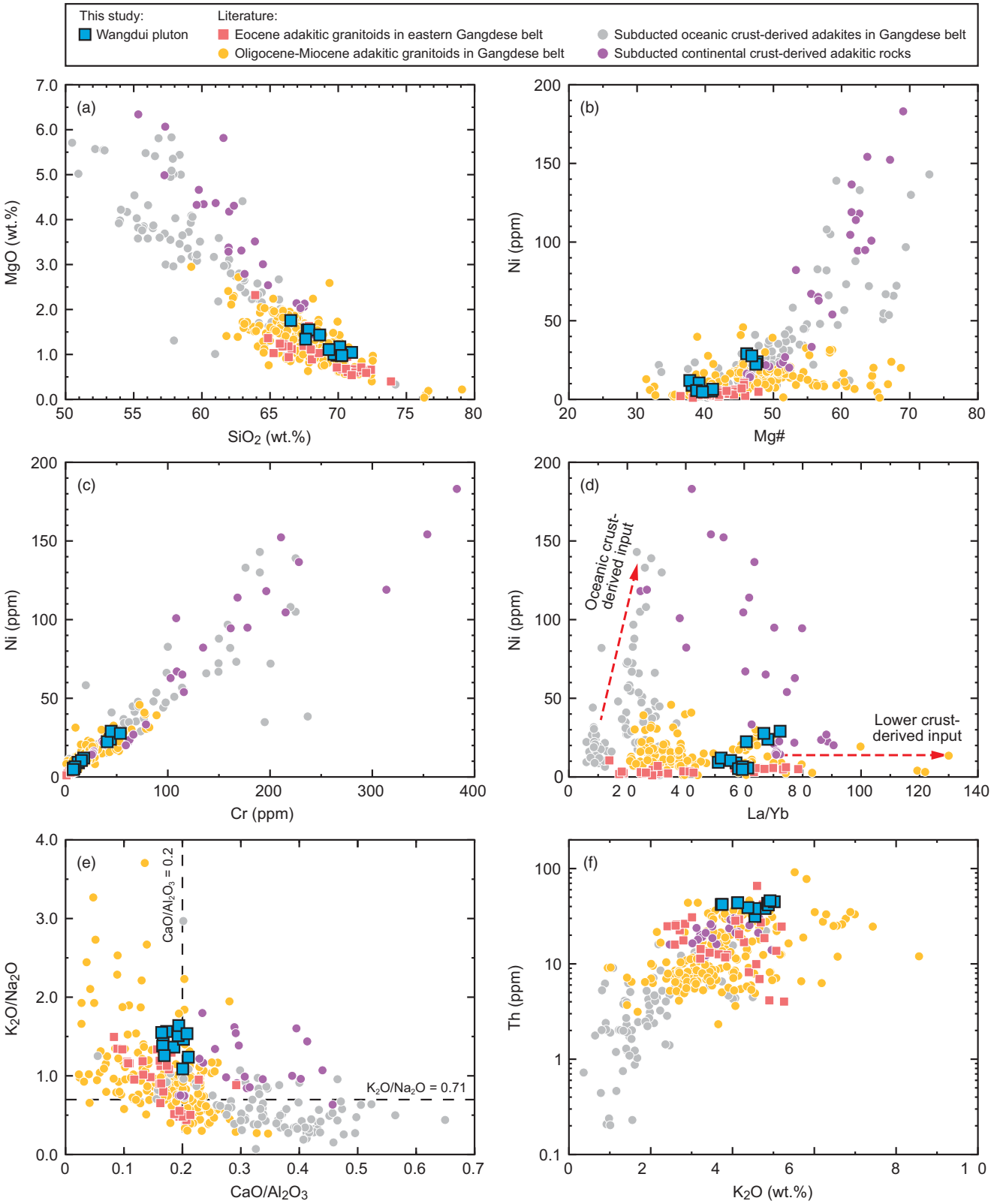

Fig. 7. (Colour online) (a) MgO vs SiO_2, (b) Ni vs Mg#, (c) Ni vs Cr, (d) Ni vs La/Yb, (e) K_2O/Na_2O vs CaO/Al_2O_3 and (f) Th vs K_2O plots for the Wangdui pluton. Data sources are the same as Figure 6.

https://doi.org/10.1017/S0016756822000206 Published online by Cambridge University Press

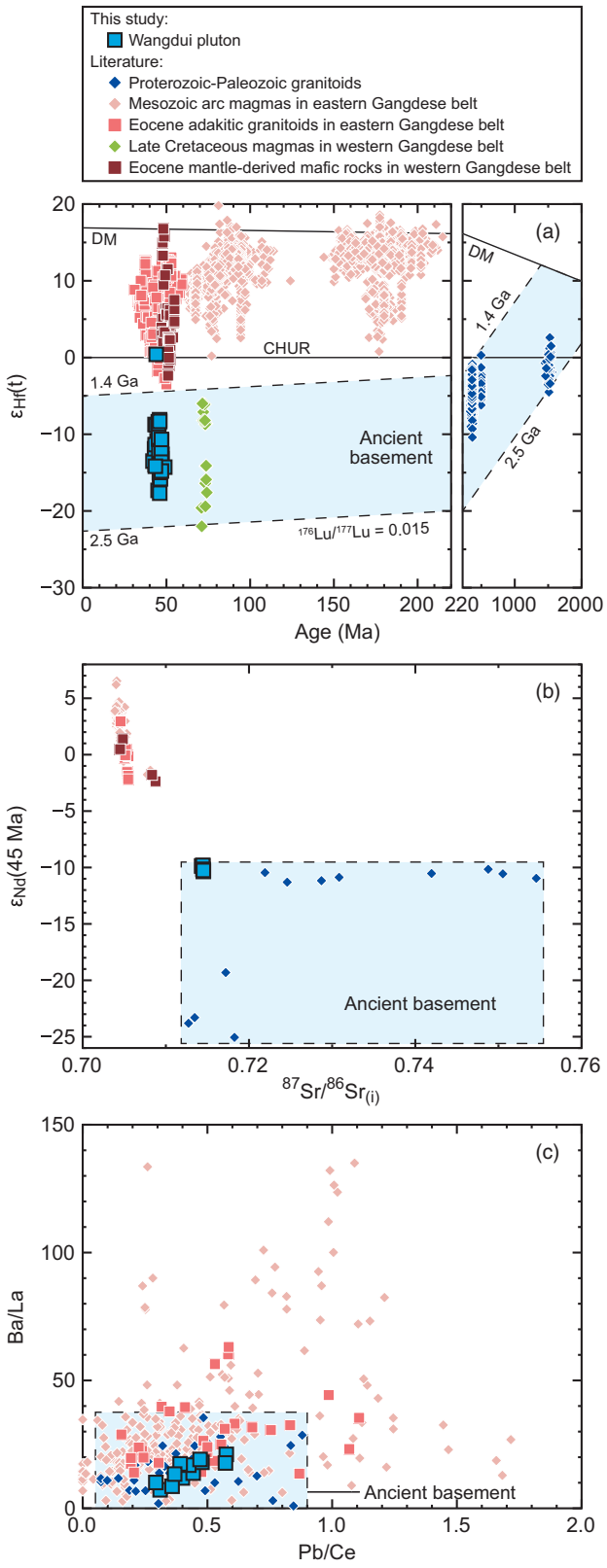

Fig. 8. (Colour online) (a) Zircon $\epsilon_{Hf}(t)$ vs U–Pb ages, (b) $\epsilon_{Nd}(t)$ vs $^{87}Sr/^{86}Sr_{(i)}$ and (c) Ba/La vs Pb/Ce plots for the Wangdui pluton. Data for Proterozoic–Palaeozoic granitoids are from Ji *et al.* (2012*b*), Dong *et al.* (2014, 2020), Dong & Zhang (2015) and Ma *et al.* (2019). Data for Mesozoic arc magmas in the eastern Gangdese belt are from Xu *et al.* (2015), Wang *et al.* (2017) and references therein. Data for Late Cretaceous magmas in the western Gangdese belt are from Jiang *et al.* (2018). Data for Eocene adakitic granitoids in the eastern Gangdese belt and mantle-derived mafic rocks in the western Gangdese belt are from the same source as Figures 4 and 6, respectively.

5.b. Nature of the magma source regions

Despite the fact that both the Eocene Wangdui adakitic pluton in the western Gangdese belt and the coeval adakitic granitoids in the eastern Gangdese belt originated from the thickened lower crust, there are some differences in the composition of elements and isotopes. This implies the presence of a heterogeneous lower-crust source beneath the Gangdese belt.

In terms of elemental composition, the Wangdui pluton has high La/Yb ratios comparable to those of the Eocene adakitic granitoids in the eastern Gangdese belt, but with relatively lower Sr contents and Sr/Y ratios (Fig. 4c, d). Additionally, the Wangdui adakitic rocks show nearly constant and highly negative Eu anomalies (Figs 5a, 6f). These geochemical features suggest the plagioclase was preserved in the residual source of Wangdui pluton. In comparison, the Eocene adakitic rocks in the eastern Gangdese belt show flat to slightly concave-upward HREE patterns (Fig. 5a) but no positive correlations of Sr/Y and La/Yb ratios with SiO_2 contents (Fig. 6d, e), indicating that the amphibole was present as a residual phase in the magmatic source rather than a crystallized phase. This difference in the residual mineral assemblage in the source region might be attributed to the role of aqueous fluids. The stability pressure of plagioclase increases with decreasing water contents, and hence it can be stable at high pressure under low water contents (Xiong *et al.* 2011). Therefore, the presence of residual plagioclase, in turn, reveals that the thickened lower-crust source of Wangdui adakitic rocks was water-poor. In contrast, since amphibole requires hydrous conditions for stability (Krawczynski *et al.* 2012), its presence suggests that the base of the continental crust of eastern Gangdese was water-rich. This interpretation is consistent with some incompatible element ratios. Because LILEs are more soluble in aqueous fluids than LREEs, Ba/La and Pb/Ce ratios are generally used to trace the metasomatism of the source region (Guo *et al.* 2005; Zheng *et al.* 2019, 2020). As shown in Figure 8c, the low Ba/La and Pb/Ce ratios of the Wangdui pluton indicate a water-poor magmatic source with limited fluid metasomatism relative to the sources of the Eocene adakitic granitoids in the eastern Gangdese belt.

In terms of isotopic composition (Fig. 8a, b), the Wangdui pluton is characterized by low negative $\epsilon_{Nd}(t)$ (−10.4 to −9.8) and high $^{87}Sr/^{86}Sr_{(i)}$ (0.7143 to 0.7145) values. Furthermore, it has low zircon $\epsilon_{Hf}(t)$ values (−17.7 to 0.4) and old Hf crustal model ages (2.24 to 1.09 Ga). These isotopic data suggest that the source region of the Wangdui adakitic rocks was dominated by ancient materials. By contrast, the Eocene adakitic rocks in the eastern Gangdese belt have relatively high $\epsilon_{Nd}(t)$ and low $^{87}Sr/^{86}Sr_{(i)}$ values, as well as high zircon $\epsilon_{Hf}(t)$ values, indicating that large amounts of juvenile materials were present in the lower crust of the eastern Gangdese belt.

The Gangdese belt was once viewed as a juvenile magmatic complex belt accreted to the southern margin of the ancient Lhasa microcontinent (Ji *et al.* 2009; Zhu *et al.* 2011). Recently, however, Proterozoic orthogneisses, Paleozoic granitoids and numerous Precambrian inherited and detrital zircons have been identified in the Gangdese belt (Ji *et al.* 2012*b*; Zheng *et al.* 2012*a*; Guo *et al.* 2016; Ma *et al.* 2019; Dong *et al.* 2020), thus indicating the existence of an ancient basement. During the Mesozoic, attributed to the northward subduction of Neo-Tethyan oceanic slab, extensive arc magmatism developed in the eastern segment of the Gangdese belt, with two activity peaks at 205–152 Ma and 109–80 Ma (e.g. Ji *et al.* 2009; Zheng *et al.* 2014; Wang *et al.* 2017; Wu *et al.* 2018). The arc magmas and associated slab-derived fluids would greatly modify the ancient basement in eastern

https://doi.org/10.1017/S0016756822000206 Published online by Cambridge University Press

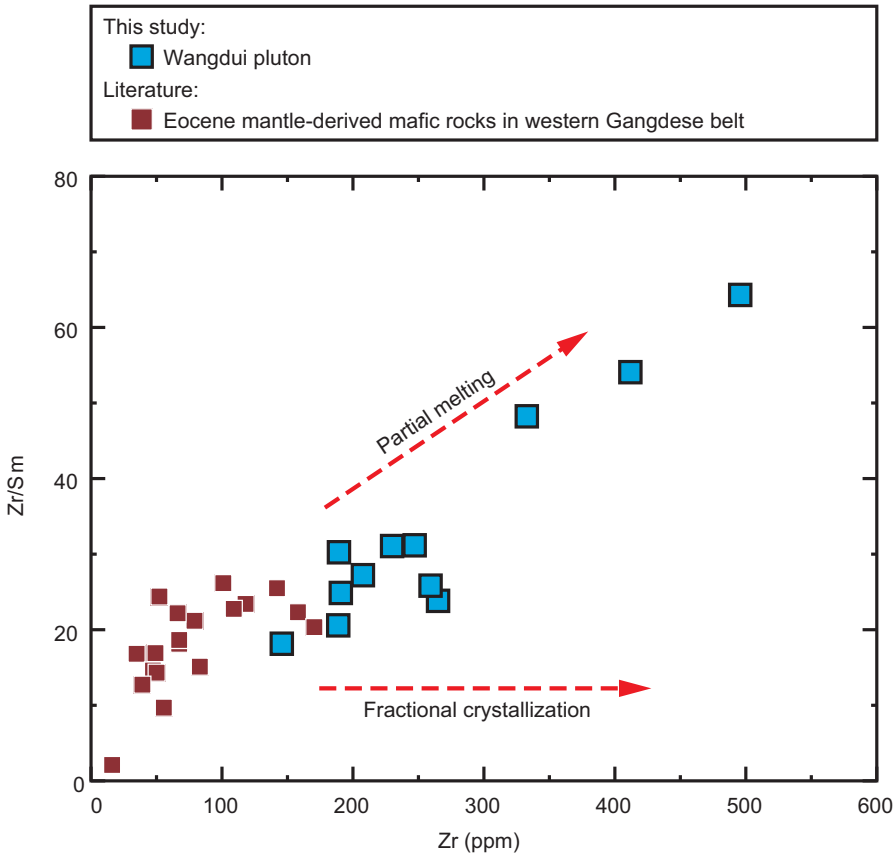

Fig. 9. (Colour online) Zr/Sm vs Zr plot (Lai *et al.* 2003) for the Wangdui pluton. Data for Eocene mantle-derived mafic rocks in the western Gangdese belt are from the same source as Figure 6.

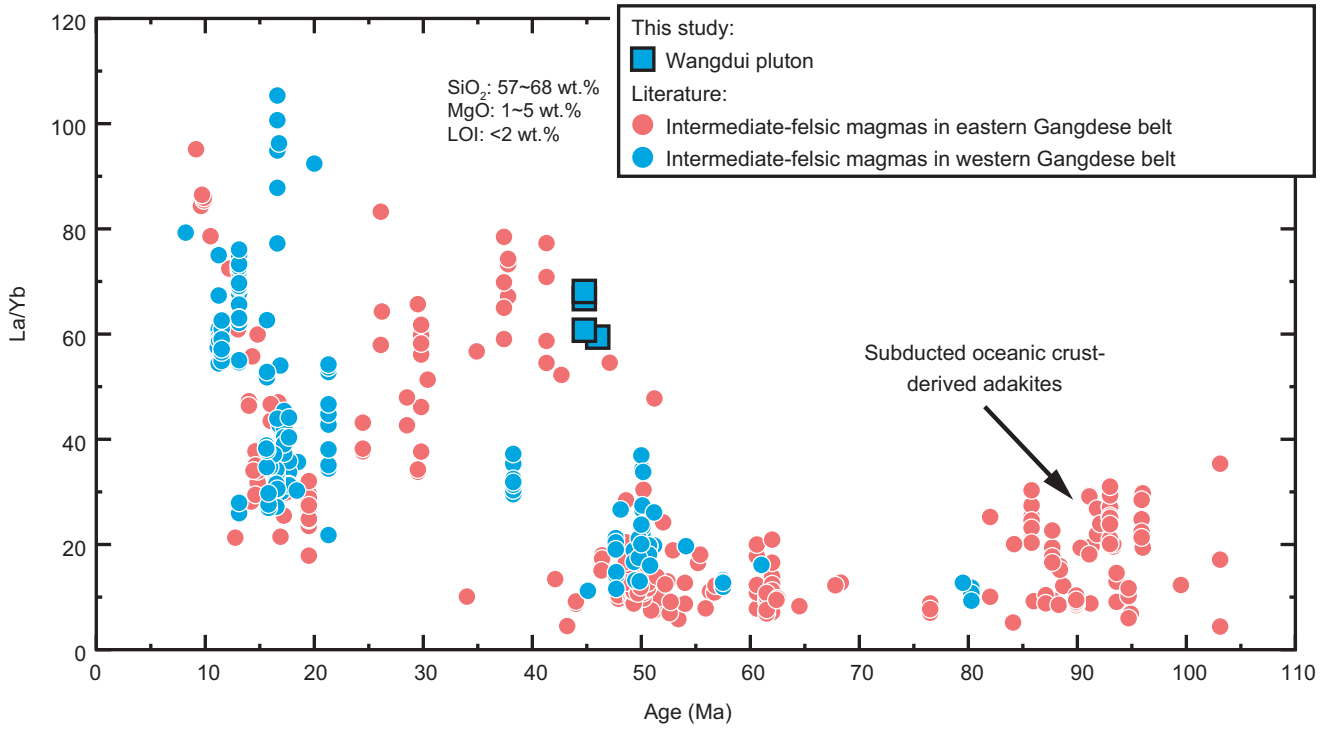

Fig. 10. (Colour online) La/Yb vs U–Pb ages plot for the Late Cretaceous–Miocene intermediate-felsic magmatic rocks in the Gangdese belt. Data and literature sources are listed in Table S2 (in the Supplementary Material available online at https://doi.org/10.1017/S0016756822000206).

https://doi.org/10.1017/S0016756822000206 Published online by Cambridge University Press

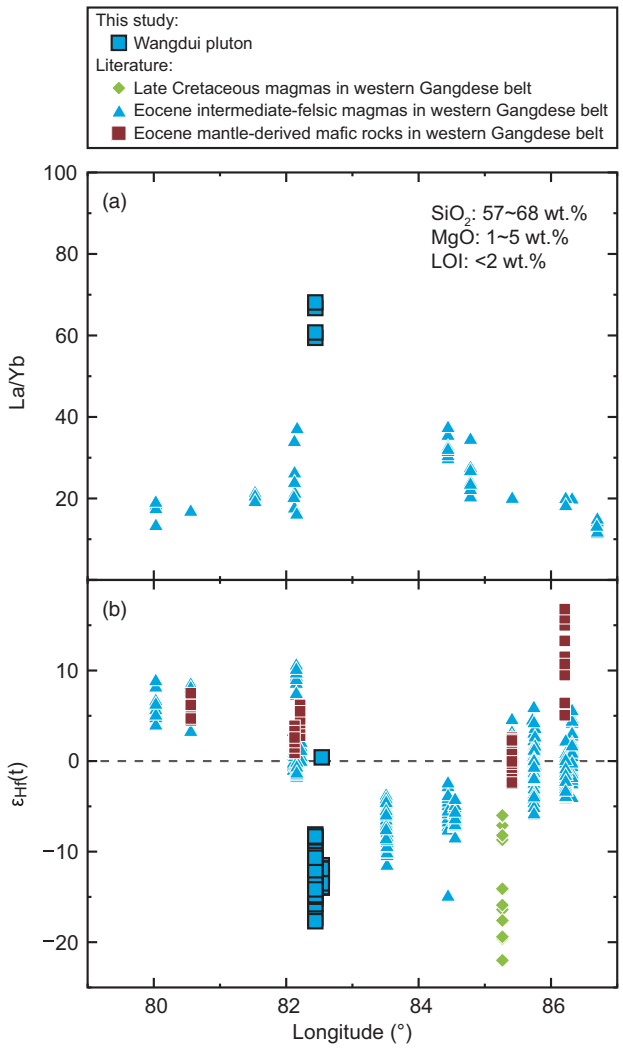

Fig. 11. (Colour online) (a) La/Yb and (b) zircon $\epsilon_{Hf}(t)$ vs longitude plots for the Eocene magmatic rocks in the western Gangdese belt. Data for intermediate-felsic magmas are from the sources listed in Table S2 (in the Supplementary Material available online at https://doi.org/10.1017/S0016756822000206) and our unpublished data. Data for Eocene mantle-derived mafic rocks and Late Cretaceous magmas are from the same source as Figures 6 and 8, respectively.

Gangdese, and eventually produce the hydrous and juvenile lower crust (Hou *et al.* 2015*b*; Hou & Wang 2019; Zheng *et al.* 2019, 2020; Dong *et al.* 2020). By contrast, the low Ba/La and Pb/Ce ratios, negative whole-rock $\epsilon_{Nd}(t)$ and zircon $\epsilon_{Hf}(t)$ values, and old crustal model ages of the studied Wangdui porphyritic monzogranites are similar to those of the Proterozoic orthogneisses and Palaeozoic granitoids (Fig. 8), implying that their magmatic source was composed predominantly of ancient Gangdese basement materials. Considering the limited development of Mesozoic arc magmatism in the western Gangdese belt (Dong, 2008; Jiang *et al.* 2018), the lack of juvenile component contribution and fluid metasomatism might cause the massive preservation of ancient basement.

5.c. Implications for crustal thickening

The Himalayan–Tibetan orogenic belt has the thickest crust on Earth (60–80 km), approximately twice the thickness of the average continental crust (Zhao *et al.* 2001; Kind *et al.* 2002). However, the timing of crustal thickening, as well as the relative contributions of tectonic shortening and magmatic underplating, remains controversial (e.g. Kapp *et al.* 2007; Mo *et al.* 2007; Volkmer *et al.* 2007; Chung *et al.* 2009; Ji *et al.* 2012*a*; Li *et al.* 2015; Ou *et al.* 2017; Zhu *et al.* 2017). The geochemical parameters of magmatic rocks are one of the approaches to estimating the crustal thickness, which matches well with the seismically determined Moho depth (Mantle & Collins 2008). As the representative parameters, La/Yb and Sr/Y ratios are widely used to track the changes of crustal thickness in magmatic arcs and collisional orogens (Chapman *et al.* 2015; Chiaradia, 2015; Hu *et al.* 2017).

In the Gangdese belt, previous studies have proposed that the crustal thickness increased dramatically in the Eocene, based on the La/Yb ratios of magmatic rocks (Ji *et al.* 2012a; Ma *et al.* 2014; Zhou *et al.* 2018). The underplating of basaltic magmas has been suggested to primarily account for this crustal thickening process since the extensive development of syn-collisional magmatism with depleted Sr–Nd–Hf isotopic compositions, including the widespread Linzizong volcanic succession, voluminous granitoid batholith and abundant mafic enclaves and gabbros (Mo *et al.* 2007; Guan *et al.* 2012; Ji *et al.* 2012*a*; Zhu *et al.* 2017; Zhou *et al.* 2018). However, the above studies mostly focused on the eastern part of the Gangdese belt, paying little attention to the western segment. It is worth noting that, unlike the eastern Gangdese lower crust which was composed predominantly of mantle-derived juvenile components, the western segment retains large amounts of ancient basement (Hou *et al.* 2013, 2015*a*; Jiang *et al.* 2018; this study). The heterogeneity of crustal composition implies that eastern and western segments underwent diverse tectonic–magmatic evolution histories, and hence there might be disparities in the timing of crustal thickening and the relative contributions of tectonic shortening and magmatic underplating.

In order to compare the crustal thickness evolution of the western and eastern Gangdese belts, we collected geochemical data concerning Late Cretaceous–Miocene magmatic rocks from both regions, and then filtered the data by SiO_2 (57–68 wt %), MgO (1–5 wt %) and loss on ignition (<2 wt %). In Figure 10, firstly, it can be observed that some Late Cretaceous rocks in the eastern Gangdese belt show relatively high La/Yb ratios. However, they are typically interpreted as the products of partial melting of subducted Neo-Tethyan oceanic crust rather than thickened continental crust, due to the geochemical characteristics of high MgO, Cr, Ni contents, and high $\epsilon_{Nd}(t)$ and $\epsilon_{Hf}(t)$ values (Zhang *et al.* 2010; Ma *et al.* 2013; Zhu *et al.* 2017; Wu *et al.* 2018). Secondly and more importantly, the La/Yb ratios of the western Gangdese magmatic rocks show a remarkable increase during *c.* 50–40 Ma, which is synchronous with the variation in the eastern Gangdese belt (Fig. 10). This indicates that the western segment experienced significant crustal thickening at a similar time to the eastern segment. In particular, the timing of western segment crustal thickening obtained here matches well with the thermochronology study. The detrital zircon fission-track data from modern river sands in the Kailas area record a rapid cooling event during the Eocene (*c.* 47–35 Ma), which has been attributed to the surface uplift and exhumation of the western Gangdese belt (Shen & Wang, 2020).

Similar to the eastern Gangdese belt, extensive Eocene magmatism also developed in the western segment, in response to the break-off of the Neo-Tethyan oceanic slab (Q Wang *et al.* 2015; R Wang *et al.* 2015). The mantle-derived mafic magmas triggered by asthenospheric upwelling would stall at the base of the

https://doi.org/10.1017/S0016756822000206 Published online by Cambridge University Press

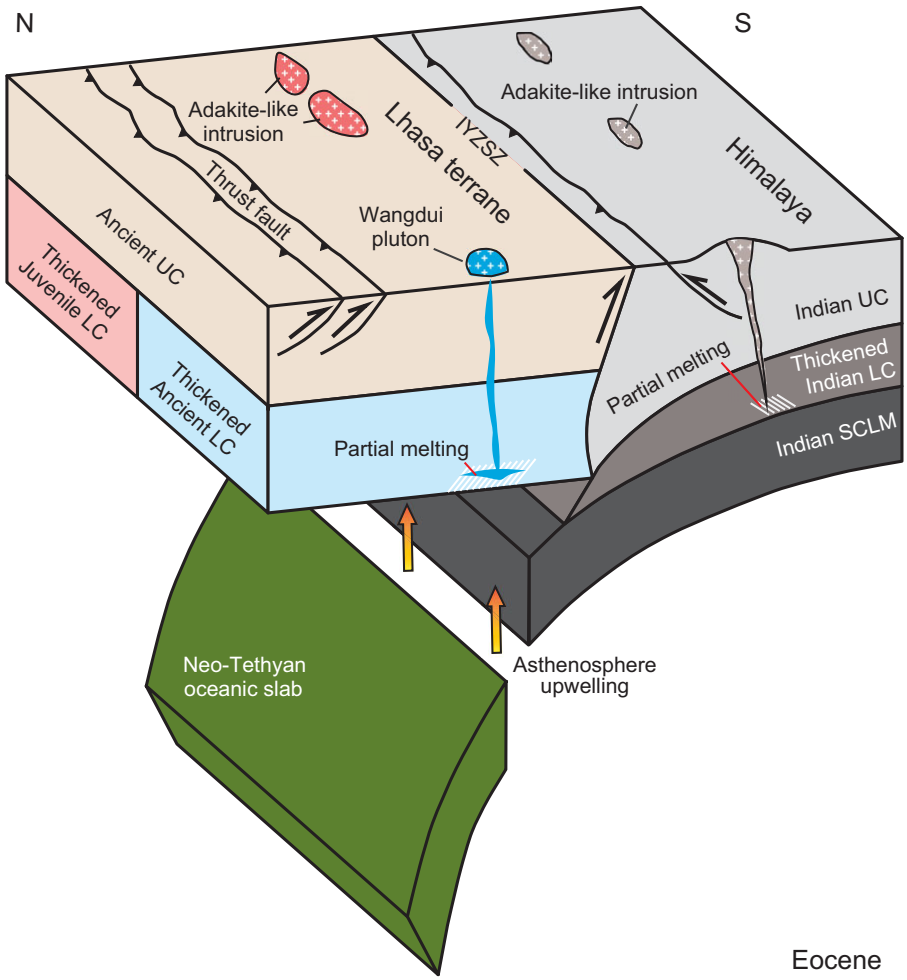

Fig. 12. (Colour online) Schematic illustration (not to scale) showing the proposed petrogenesis of Eocene Wangdui adakitic rocks (modified from Zheng *et al.* 2020). Abbreviations: IYZSZ = Indus–Yarlung Zangbo suture zones; LC = lower crust; SCLM = sub-continental lithospheric mantle; UC = upper crust.

continental crust, where they interacted with the ancient basement and provided sufficient heat to induce crustal melting. As a result of the crust–mantle interaction, the isotopic compositions of the Eocene magmatic rocks in the western Gangdese belt show wide variations, ranging between those of the most depleted mantle-derived mafic rocks and those of the pre-collisional Late Cretaceous ancient basement-derived magmas (Fig. 11). However, in contrast to that the Eocene adakitic granitoids in the eastern Gangdese belt have juvenile Sr–Nd–Hf isotopic compositions, and the Wangdui pluton which has the highest La/Yb ratios in the western segment is characterized by the most negative zircon $\epsilon_{Hf}(t)$ values. This suggests that the thickened lower crust beneath the western Gangdese belt was composed predominantly of ancient basement materials. In this case, the underplating of juvenile mantle-derived magmas is unsuitable to account for the crustal thickening of the ancient basement; instead, tectonic shortening might play a more crucial role (Fig. 12).

In fact, the thickened lower-crust-derived adakitic rocks began to appear during the Eocene, not only along the Gangdese belt but also in the Tethyan Himalaya and Qiangtang terranes (Zeng *et al.* 2011; Hou *et al.* 2012; Long *et al.* 2015; Ou *et al.* 2017). Such a widespread distribution indicates that the central Himalayan–Tibetan orogen experienced crustal thickening as a whole in this period. This inference is supported by other studies. Since the disappearance of marine strata can constrain the onset of plateau uplift, the youngest marine strata in the Tethyan Himalaya are Early Eocene in age, suggesting that the uplift was active during the Eocene (Wang *et al.* 2014). As for the Lhasa and Qiangtang terranes, published thermochronological data show an exhumation peak at *c.* 55–35 Ma, also indicating an Eocene rapid uplift (Rohrmann *et al.* 2012; Dai *et al.* 2013; Shen & Wang 2020). Furthermore, the above adakitic rocks in Tethyan Himalaya and Qiangtang terranes show enriched Sr–Nd–Hf isotopic compositions, consistent with the Wangdui pluton in the western Gangdese belt. This implies that the underplating of mantle-derived magmas might have a limited effect on crustal thickening there, while tectonic shortening might have more. Plate reconstructions show that there was a strong convergence after the India–Asia continental collision in the Early Eocene, which resulted in the extensive development of fold–thrust belts in the central Himalayan–Tibetan orogen (van Hinsbergen *et al.* 2011; Li *et al.* 2015). These fold–thrust belts, in turn, would accommodate most of the convergence and lead to the crustal shortening and thickening (Wang *et al.* 2014; Li *et al.* 2015 and references therein). Therefore, we believe that the Eocene crustal thickening of the central Himalayan–Tibetan orogen might be primarily caused by tectonic shortening rather than mantle-derived magma underplating.

6. Conclusions

(1) The Wangdui porphyritic monzogranites in the western Gangdese belt were emplaced at *c.* 46–44 Ma and show geochemical affinities with adakites. Similar to the previously

https://doi.org/10.1017/S0016756822000206 Published online by Cambridge University Press

reported coeval adakitic rocks in the eastern Gangdese belt, the Wangdui pluton was also most likely produced by partial melting of the thickened lower crust. However, in contrast to the juvenile lower-crust source in the eastern segment, the magmatic source of Wangdui pluton was composed predominantly of ancient basement materials, revealing the east–west-trending heterogeneity of lower-crustal composition in the Gangdese belt.

(2) The La/Yb ratios of magmatic rocks suggest that both the western and eastern Gangdese belts experienced significant crustal thickening in the Eocene. However, the disparity in crustal composition implies that these two regions have diverse tectonic–magmatic evolution processes and different thickening mechanisms. Unlike the crustal thickening caused by the underplating of juvenile mantle-derived magmas in the eastern segment, the tectonic shortening might play a more crucial role in the western segment. In fact, the Eocene adakitic rocks, which were derived from thickened lower crust and have enriched isotopic compositions, are widely distributed in the central Himalayan–Tibetan orogen. This, in combination with the extensive development of fold–thrust belts, suggests that tectonic shortening might be the main mechanism accounting for the crustal thickening associated with the India–Asia continental collision.

Supplementary material. To view supplementary material for this article, please visit https://doi.org/10.1017/S0016756822000206

Acknowledgements. This work was funded by the National Key Research and Development Program of China (grants 2019YFA0708602, 2016YFC0600310), the National Natural Science Foundation of China (grants 42022014, 41872083, 41472076), the Program of the China Geological Survey (DD20160024-07, DD20179172), the China Fundamental Research Funds for the Central Universities (grant 2652018133), and the 111 Project of the Ministry of Science and Technology (grant BP0719021).

Conflict of interest. The authors declare that they have no known competing financial interests or personal relationships that could have appeared to influence the work reported in this paper.

References

Andersen T (2002) Correction of common lead in U–Pb analyses that do not report ^{204}Pb. *Chemical Geology* **192**, 59–79.

Atherton MP and Petford N (1993) Generation of sodium-rich magmas from newly underplated basaltic crust. *Nature* **362**, 144–6.

Blichert-Toft J and Albarède F (1997) The Lu-Hf isotope geochemistry of chondrites and the evolution of the mantle-crust system. *Earth and Planetary Science Letters* **148**, 243–58.

Castillo PR, Janney PE and Solidum RU (1999) Petrology and geochemistry of Camiguin Island, southern Philippines: insights to the source of adakites and other lavas in a complex arc setting. *Contributions to Mineralogy and Petrology* **134**, 33–51.

Chapman JB, Ducea MN, DeCelles PG and Profeta L (2015) Tracking changes in crustal thickness during orogenic evolution with Sr/Y: an example from the North American Cordillera. *Geology* **43**, 919–22.

Chen JL, Wu JB, Xu JF, Dong YH, Wang BD and Kang ZQ (2013) Geochemistry of Eocene high-Mg# adakitic rocks in the northern Qiangtang terrane, central Tibet: implications for early uplift of the plateau. *GSA Bulletin* **125**, 1800–19.

Chen JL, Xu JF, Zhao WX, Dong YH, Wang BD and Kang ZQ (2011) Geochemical variations in Miocene adakitic rocks from the western and eastern Lhasa terrane: implications for lower crustal flow beneath the Southern Tibetan Plateau. *Lithos* **125**, 928–39.

Chen L, Qin KZ, Li GM, Li JX, Xiao B, Zhao JX and Fan X (2015) Zircon U–Pb ages, geochemistry, and Sr–Nd–Pb–Hf isotopes of the Nuri intrusive rocks in the Gangdese area, southern Tibet: constraints on timing, petrogenesis, and tectonic transformation. *Lithos* **212–215**, 379–96.

Chen PR, Hua RM, Zhang BT, Lu JJ and Fan CF (2002) Early Yanshanian post-orogenic granitoids in the Nanling region. *Science in China Series D: Earth Sciences* **45**, 755–68.

Chen YH, Yang JS, Xiong FH, Zhang L, Lai SM and Chen M (2015) Geochronology and geochemistry of the subduction-related rocks with high Sr/Y ratios in the Zedong area: implications for the magmatism in southern Lhasa terrane during Late Cretaceous. *Acta Geologica Sinica (English edition)* **89**, 351–68.

Chiaradia M (2015) Crustal thickness control on Sr/Y signatures of recent arc magmas: an Earth scale perspective. *Scientific Reports* **5**, 8115.

Chung SL, Chu MF, Ji JQ, O'Reilly SY, Pearson NJ, Liu DY, Lee TY and Lo CH (2009) The nature and timing of crustal thickening in Southern Tibet: geochemical and zircon Hf isotopic constraints from postcollisional adakites. *Tectonophysics* **477**, 36–48.

Chung SL, Liu DY, Ji JQ, Chu MF, Lee HY, Wen DJ, Lo CH, Lee TY, Qian Q and Zhang Q (2003) Adakites from continental collision zones: melting of thickened lower crust beneath southern Tibet. *Geology* **31**, 1021–4.

Dai JG, Wang CS, Hourigan J, Li ZJ and Zhuang GS (2013) Exhumation history of the Gangdese batholith, southern Tibetan Plateau: evidence from apatite and zircon (U-Th)/He thermochronology. *The Journal of Geology* **121**, 155–72.

Defant MJ and Drummond MS (1990) Derivation of some modern arc magmas by melting of young subducted lithosphere. *Nature* **347**, 662–5.

Ding HX, Zhang ZM, Dong X, Tian Z, Xiang H, Mu HC, Gou ZB, Shui XF, Li WC and Mao LJ (2016) Early Eocene (c. 50 Ma) collision of the Indian and Asian continents: constraints from the North Himalayan metamorphic rocks, southeastern Tibet. *Earth and Planetary Science Letters* **435**, 64–73.

Ding L, Spicer RA, Yang J, Xu Q, Cai FL, Li S, Lai QZ, Wang HQ, Spicer TEV, Yue YH, Shukla A, Srivastava G, Khan MA, Bera S and Mehrotra R (2017) Quantifying the rise of the Himalaya orogen and implications for the South Asian monsoon. *Geology* **45**, 215–18.

Dong GC, Mo XX, Zhao ZD, Zhu DC, Xie XF and Dong ML (2011) The Neocene magmatism from Namuru intrusion in western Gangdese, Tibet and its tectonic significance. *Acta Petrologica Sinica* **27**, 1983–92 (in Chinese with English abstract).

Dong X (2008) *The geochronology and geochemistry of the Mesozoic and Cenozoic granitoids from southwestern Gangdese belt, Tibet*. MSc thesis, China University of Geosciences, Beijing. Published thesis.

Dong X and Zhang ZM (2015) Cambrian granitoids from the southeastern Tibetan Plateau: research on petrology and zircon Hf isotope. *Acta Petrologica Sinica* **31**, 1183–99 (in Chinese with English abstract).

Dong X, Zhang ZM, Liu F, He ZY and Lin YH (2014) Late Paleozoic intrusive rocks from the southeastern Lhasa terrane, Tibetan Plateau, and their Late Mesozoic metamorphism and tectonic implications. *Lithos* **198–199**, 249–62.

Dong X, Zhang ZM, Niu YL, Tian ZL and Zhang LL (2020) Reworked Precambrian metamorphic basement of the Lhasa terrane, southern Tibet: zircon/titanite U–Pb geochronology, Hf isotope and geochemistry. *Precambrian Research* **336**, 105496.

Dupont-Nivet G, Krijgsman W, Langereis CG, Abels HA, Dai S and Fang XM (2007) Tibetan plateau aridification linked to global cooling at the Eocene–Oligocene transition. *Nature* **445**, 635–8.

Gao R, Lu ZW, Klemperer SL, Wang HY, Dong SW, Li WH and Li HQ (2016) Crustal-scale duplexing beneath the Yarlung Zangbo suture in the western Himalaya. *Nature Geoscience* **9**, 555–60.

Gou LL, Zhang LF, Tao RB and Du JX (2012) A geochemical study of syn-subduction and post-collisional granitoids at Muzhaerte River in the Southwest Tianshan UHP belt, NW China. *Lithos* **136–139**, 201–24.

Griffin WL, Pearson NJ, Belousova E, Jackson SE, van Achterbergh E, O'Reilly SY and Shee SR (2000) The Hf isotope composition of cratonic mantle: LAM-MC-ICPMS analysis of zircon megacrysts in kimberlites. *Geochimica et Cosmochimica Acta* **64**, 133–47.

Griffin WL, Powell WJ, Pearson NJ and O'Reilly SY (2008) GLITTER: data reduction software for laser ablation ICP-MS. In *Laser Ablation-ICP-MS in the Earth Sciences: Current Practices and Outstanding Issues* (ed. P Sylvester), pp. 204–7. Quebec City: Mineralogical Association of Canada Short Course Series 40.

Guan Q, Zhu DC, Zhao ZD, Dong GC, Zhang LL, Li XW, Liu M, Mo XX, Liu YS and Yuan HL (2012) Crustal thickening prior to 38 Ma in southern Tibet: evidence from lower crust-derived adakitic magmatism in the Gangdese Batholith. *Gondwana Research* **21**, 88–99.

Guo F, Nakamuru E, Fan W, Kobayoshi K and Li C (2007a) Generation of Palaeocene adakitic andesites by magma mixing; Yanji Area, NE China. *Journal of Petrology* **48**, 661–92.

Guo L, Zhang HF, Harris N, Xu WC and Pan FB (2016) Late Devonian-Early Carboniferous magmatism in the Lhasa terrane and its tectonic implications: evidences from detrital zircons in the Nyingchi Complex. *Lithos* **245**, 47–59.

Guo ZF, Hertogen J, Liu JQ, Pasteels P, Boven A, Punzalan L, He HY, Luo XJ and Zhang WH (2005) Potassic magmatism in western Sichuan and Yunnan provinces, SE Tibet, China: petrological and geochemical constraints on petrogenesis. *Journal of Petrology* **46**, 33–78.

Guo ZF, Wilson M and Liu JQ (2007b) Post-collisional adakites in south Tibet: products of partial melting of subduction-modified lower crust. *Lithos* **96**, 205–24.

Harris N (2006) The elevation history of the Tibetan Plateau and its implications for the Asian monsoon. *Palaeogeography, Palaeoclimatology, Palaeoecology* **241**, 4–15.

Hoskin PWO and Schaltegger U (2003) The composition of zircon and igneous and metamorphic petrogenesis. *Reviews in Mineralogy and Geochemistry* **53**, 27–62.

Hou ZQ and Cook NJ (2009) Metallogenesis of the Tibetan collisional orogen: a review and introduction to the special issue. *Ore Geology Reviews* **36**, 2–24.

Hou ZQ, Duan LF, Lu YJ, Zheng YC, Zhu DC, Yang ZM, Yang ZS, Wang BD, Pei YR and Zhao ZD (2015a) Lithospheric architecture of the Lhasa terrane and its control on ore deposits in the Himalayan-Tibetan orogen. *Economic Geology* **110**, 1541–75.

Hou ZQ, Gao YF, Qu XM, Rui ZY and Mo XX (2004) Origin of adakitic intrusives generated during mid-Miocene east–west extension in southern Tibet. *Earth and Planetary Science Letters* **220**, 139–55.

Hou ZQ and Wang R (2019) Fingerprinting metal transfer from mantle. *Nature Communications* **10**, 3510.

Hou ZQ, Yang ZM, Lu YJ, Kemp A, Zheng YC, Li QY, Tang JX, Yang ZS and Duan LF (2015b) A genetic linkage between subduction- and collision-related porphyry Cu deposits in continental collision zones. *Geology* **43**, 247–50.

Hou ZQ, Zheng YC, Yang ZM, Rui ZY, Zhao ZD, Jiang SH, Qu XM and Sun QZ (2013) Contribution of mantle components within juvenile lower-crust to collisional zone porphyry Cu systems in Tibet. *Mineralium Deposita* **48**, 173–92.

Hou ZQ, Zheng YC, Zeng LS, Gao LE, Huang KX, Li W, Li QY, Fu Q, Liang W and Sun QZ (2012) Eocene–Oligocene granitoids in southern Tibet: constraints on crustal anatexis and tectonic evolution of the Himalayan orogen. *Earth and Planetary Science Letters* **349–350**, 38–52.

Hu FY, Ducea MN, Liu SW and Chapman JB (2017) Quantifying crustal thickness in continental collisional belts: global perspective and a geologic application. *Scientific Reports* **7**, 7058.

Hu YB, Liu JQ, Ling MX, Ding W, Liu Y, Zartman RE, Ma XF, Liu DY, Zhang CC, Sun SJ, Zhang LP, Wu K and Sun WD (2015) The formation of Qulong adakites and their relationship with porphyry copper deposit: geochemical constraints. *Lithos* **220–223**, 60–80.

Ji WQ, Wu FY, Chung SL, Li JX and Liu CZ (2009) Zircon U–Pb geochronology and Hf isotopic constraints on petrogenesis of the Gangdese batholith, southern Tibet. *Chemical Geology* **262**, 229–45.

Ji WQ, Wu FY, Chung SL and Liu CZ (2012b) Identification of early Carboniferous granitoids from southern Tibet and implications for terrane assembly related to the Paleo-Tethyan evolution. *The Journal of Geology* **120**, 531–41.

Ji WQ, Wu FY, Liu CZ and Chung SL (2012a) Early Eocene crustal thickening in southern Tibet: new age and geochemical constraints from the Gangdese batholith. *Journal of Asian Earth Sciences* **53**, 82–95.

Jiang JS, Zheng YY, Gao SB, Zhang YC, Huang J, Liu J, Wu S, Xu J and Huang LL (2018) The newly-discovered Late Cretaceous igneous rocks in the Nuocang district: products of ancient crust melting triggered by Neo-Tethyan slab rollback in the western Gangdese. *Lithos* **308–309**, 294–315.

Jiang ZQ, Wang Q, Li ZX, Wyman DA, Tang GJ, Jia XH and Yang YH (2012) Late Cretaceous (ca. 90 Ma) adakitic intrusive rocks in the Kelu area, Gangdese Belt (southern Tibet): slab melting and implications for Cu–Au mineralization. *Journal of Asian Earth Sciences* **53**, 67–81.

Jiang ZQ, Wang Q, Wyman DA, Li ZX, Yang JH, Shi XB, Ma L, Tang GJ, Gou GN, Jia XH and Guo HF (2014) Transition from oceanic to continental lithosphere subduction in southern Tibet: evidence from the Late Cretaceous–early Oligocene (91–30 Ma) intrusive rocks in the Chanang–Zedong area, southern Gangdese. *Lithos* **196–197**, 213–31.

Kang ZQ, Xu JF, Wilde SA, Feng ZH, Chen JL, Wang BD, Fu WC and Pan HB (2014) Geochronology and geochemistry of the Sangri Group volcanic rocks, Southern Lhasa Terrane: implications for the early subduction history of the Neo-Tethys and Gangdese Magmatic Arc. *Lithos* **200–201**, 157–68.

Kapp P, DeCelles PG, Leier A, Fabijanic J, He S, Pullen A, Gehrels GE and Ding L (2007) The Gangdese retroarc thrust belt revealed. *GSA Today* **17**, 4.

Karsli O, Dokuz A, Kandemir R, Aydin F, Schmitt AK, Ersoy EY and Alyıldız C (2019) Adakite-like parental melt generation by partial fusion of juvenile lower crust, Sakarya Zone, NE Turkey: a far-field response to break-off of the southern Neotethyan oceanic lithosphere. *Lithos* **338–339**, 58–72.

Karsli O, Ketenci M, Uysal İ, Dokuz A, Aydin F, Chen B, Kandemir R and Wijbrans J (2011) Adakite-like granitoid porphyries in the Eastern Pontides, NE Turkey: potential parental melts and geodynamic implications. *Lithos* **127**, 354–72.

Keller CB, Schoene B, Barboni M, Samperton KM and Husson JM (2015) Volcanic–plutonic parity and the differentiation of the continental crust. *Nature* **523**, 301–7.

Keto LS and Jacobsen SB (1987) Nd and Sr isotopic variations of Early Paleozoic oceans. *Earth and Planetary Science Letters* **84**, 27–41.

Kind R, Yuan X, Saul J, Nelson D, Sobolev SV, Mechie J, Zhao W, Kosarev G, Ni J, Achauer U and Jiang M (2002) Seismic images of crust and upper mantle beneath Tibet: evidence for Eurasian plate subduction. *Science* **298**, 1219–21.

Krawczynski MJ, Grove TL and Behrens H (2012) Amphibole stability in primitive arc magmas: effects of temperature, H_2O content, and oxygen fugacity. *Contributions to Mineralogy and Petrology* **164**, 317–39.

Lai SC, Liu CY and Yi HS (2003) Geochemistry and petrogenesis of Cenozoic andesite-dacite associations from the Hoh Xil region, Tibetan Plateau. *International Geology Review* **45**, 998–1019.

Li SM, Zhu DC, Wang Q, Zhao ZD, Zhang LL, Liu SA, Chang QS, Lu YH, Dai JG and Zheng YC (2016) Slab-derived adakites and subslab asthenosphere-derived OIB-type rocks at 156 ± 2 Ma from the north of Gerze, central Tibet: records of the Bangong–Nujiang oceanic ridge subduction during the Late Jurassic. *Lithos* **262**, 456–69.

Li YL, Li XH, Wang CS, Wei YS, Chen X, He J, Xu M and Hou YL (2017) Miocene adakitic intrusions in the Zhongba terrane: implications for the origin and geochemical variations of post-collisional adakitic rocks in southern Tibet. *Gondwana Research* **41**, 65–76.

Li YL, Wang CS, Dai JG, Xu GQ, Hou YL and Li XH (2015) Propagation of the deformation and growth of the Tibetan–Himalayan orogen: a review. *Earth-Science Reviews* **143**, 36–61.

Long XP, Wilde SA, Wang Q, Yuan C, Wang XC, Li J, Jiang ZQ and Dan W (2015) Partial melting of thickened continental crust in central Tibet: evidence from geochemistry and geochronology of Eocene adakitic rhyolites in the northern Qiangtang Terrane. *Earth and Planetary Science Letters* **414**, 30–44.

Ludwig K (2003) *Isoplot v. 3.0: A Geochronological Toolkit for Microsoft Excel*. Berkeley, California: Berkeley Geochronology Center.

Ma L, Kerr AC, Wang Q, Jiang ZQ, Tang GJ, Yang JH, Xia XP, Hu WL, Yang ZY and Sun P (2019) Nature and evolution of crust in southern Lhasa, Tibet: transformation from microcontinent to juvenile terrane. *Journal of Geophysical Research: Solid Earth* **124**, 6452–74.

Ma L, Wang BD, Jiang ZQ, Wang Q, Li ZX, Wyman DA, Zhao SR, Yang JH, Gou GN and Guo HF (2014) Petrogenesis of the Early Eocene adakitic rocks in the Napuri area, southern Lhasa: partial melting of thickened lower crust

https://doi.org/10.1017/S0016756822000206 Published online by Cambridge University Press

during slab break-off and implications for crustal thickening in southern Tibet. *Lithos* **196–197**, 321–38.

Ma L, Wang Q, Wyman DA, Li ZX, Jiang ZQ, Yang JH, Gou GN and Guo HF (2013) Late Cretaceous (100–89 Ma) magnesian charnockites with adakitic affinities in the Milin area, eastern Gangdese: partial melting of subducted oceanic crust and implications for crustal growth in southern Tibet. *Lithos* **175–176**, 315–32.

Macpherson CG, Dreher ST and Thirlwall MF (2006) Adakites without slab melting: high pressure differentiation of island arc magma, Mindanao, the Philippines. *Earth and Planetary Science Letters* **243**, 581–93.

Mantle GW and Collins WJ (2008) Quantifying crustal thickness variations in evolving orogens: correlation between arc basalt composition and Moho depth. *Geology* **36**, 87–90.

Mo XX, Hou ZQ, Niu YL, Dong GC, Qu XM, Zhao ZD and Yang ZM (2007) Mantle contributions to crustal thickening during continental collision: evidence from Cenozoic igneous rocks in southern Tibet. *Lithos* **96**, 225–42.

Mo XX, Niu YL, Dong GC, Zhao ZD, Hou ZQ, Zhou S and Ke S (2008) Contribution of syncollisional felsic magmatism to continental crust growth: a case study of the Paleogene Linzizong volcanic Succession in southern Tibet. *Chemical Geology* **250**, 49–67.

Nábělek J, Hetényi G, Vergne J, Sapkota S, Kafle B, Jiang M, Su HP, Chen J, Huang B-S and the Hi-CLIMB Team (2009) Underplating in the Himalaya-Tibet collision zone revealed by the Hi-CLIMB experiment. *Science* **325**, 1371–74.

Ou Q, Wang Q, Wyman DA, Zhang HX, Yang JH, Zeng JP, Hao LL, Chen YW, Liang H and Qi Y (2017) Eocene adakitic porphyries in the central-northern Qiangtang Block, central Tibet: partial melting of thickened lower crust and implications for initial surface uplifting of the plateau. *Journal of Geophysical Research: Solid Earth* **122**, 1025–53.

Pang KN, Chung SL, Zarrinkoub MH, Li XH, Lee HY, Lin TH and Chiu HY (2016) New age and geochemical constraints on the origin of Quaternary adakite-like lavas in the Arabia–Eurasia collision zone. *Lithos* **264**, 348–59.

Peccerillo A and Taylor SR (1976) Geochemistry of Eocene calc-alkaline volcanic rocks from the Kastamonu area, Northern Turkey. *Contributions to Mineralogy and Petrology* **58**, 63–81.

Rapp RP, Shimizu N, Norman MD and Applegate GS (1999) Reaction between slab-derived melts and peridotite in the mantle wedge: experimental constraints at 3.8 GPa. *Chemical Geology* **160**, 335–56.

Rohrmann A, Kapp P, Carrapa B, Reiners PW, Guynn J, Ding L and Heizler M (2012) Thermochronologic evidence for plateau formation in central Tibet by 45 Ma. *Geology* **40**, 187–90.

Shafiei B, Haschke M and Shahabpour J (2009) Recycling of orogenic arc crust triggers porphyry Cu mineralization in Kerman Cenozoic arc rocks, southeastern Iran. *Mineralium Deposita* **44**, 265–83.

Shen TY and Wang GC (2020) Detrital zircon fission-track thermochronology of the present-day river drainage system in the Mt. Kailas area, western Tibet: implications for multiple cooling stages of the Gangdese magmatic arc. *Journal of Earth Science* **31**, 896–904.

Söderlund U, Patchett PJ, Vervoort JD and Isachsen CE (2004) The ^{176}Lu decay constant determined by Lu–Hf and U–Pb isotope systematics of Precambrian mafic intrusions. *Earth and Planetary Science Letters* **219**, 311–24.

Song SG, Niu YL, Wei CJ, Ji JQ and Su L (2010) Metamorphism, anatexis, zircon ages and tectonic evolution of the Gongshan block in the northern Indochina continent – an eastern extension of the Lhasa Block. *Lithos* **120**, 327–46.

Stern CR and Kilian R (1996) Role of the subducted slab, mantle wedge and continental crust in the generation of adakites from the Andean Austral Volcanic Zone. *Contributions to Mineralogy and Petrology* **123**, 263–81.

Streck MJ, Leeman WP and Chesley J (2007) High-magnesian andesite from Mount Shasta: a product of magma mixing and contamination, not a primitive mantle melt. *Geology* **35**, 351–4.

Sun SS and McDonough WF (1989) Chemical and isotopic systematics of oceanic basalts: implications for mantle composition and processes. In *Magmatism in the Ocean Basins* (eds AD Saunders & MJ Norry), pp. 313–45. Geological Society of London, Special Publication no. 42.

Sun WD, Ling MX, Chung SL, Ding X, Yang XY, Liang HY, Fan WM, Goldfarb R and Yin QZ (2012) Geochemical constraints on adakites of different origins and copper mineralization. *The Journal of Geology* **120**, 105–20.

Sun X, Lu YJ, McCuaig TC, Zheng YY, Chang HF, Guo F and Xu LJ (2018) Miocene ultrapotassic, high-Mg dioritic, and adakite-like rocks from Zhunuo in Southern Tibet: implications for mantle metasomatism and porphyry copper mineralization in collisional orogens. *Journal of Petrology* **59**, 341–86.

Topuz G, Altherr R, Schwarz WH, Siebel W, Satır M and Dokuz A (2005) Post-collisional plutonism with adakite-like signatures: the Eocene Saraycık granodiorite (Eastern Pontides, Turkey). *Contributions to Mineralogy and Petrology* **150**, 441–55.

van Hinsbergen DJJ, Steinberger B, Doubrovine PV and Gassmöller R (2011) Acceleration and deceleration of India-Asia convergence since the Cretaceous: roles of mantle plumes and continental collision. *Journal of Geophysical Research: Solid Earth* **116**, B06101.

Volkmer JE, Kapp P, Guynn JH and Lai QZ (2007) Cretaceous-Tertiary structural evolution of the north central Lhasa terrane, Tibet. *Tectonics* **26**.

Wang C, Ding L, Zhang LY, Kapp P, Pullen A and Yue YH (2016) Petrogenesis of middle–late Triassic volcanic rocks from the Gangdese belt, southern Lhasa terrane: implications for early subduction of Neo-Tethyan oceanic lithosphere. *Lithos* **262**, 320–33.

Wang CS, Dai JG, Zhao XX, Li YL, Graham SA, He DF, Ran B and Meng J (2014) Outward-growth of the Tibetan Plateau during the Cenozoic: a review. *Tectonophysics* **621**, 1–43.

Wang Q, Wyman DA, Xu JF, Dong YH, Vasconcelos PM, Pearson N, Wan YS, Dong H, Li CF, Yu YS, Zhu TX, Feng XT, Zhang QY, Zi F and Chu ZY (2008) Eocene melting of subducting continental crust and early uplifting of central Tibet: evidence from central-western Qiangtang high-K calc-alkaline andesites, dacites and rhyolites. *Earth and Planetary Science Letters* **272**, 158–71.

Wang Q, Xu JF, Jian P, Bao ZW, Zhao ZH, Li CF, Xiong XL and Ma JL (2006) Petrogenesis of adakitic porphyries in an extensional tectonic setting, Dexing, South China: implications for the genesis of porphyry copper mineralization. *Journal of Petrology* **47**, 119–44.

Wang Q, Zhu DC, Cawood PA, Zhao ZD, Liu SA, Chung SL, Zhang LL, Liu D, Zheng YC and Dai JG (2015) Eocene magmatic processes and crustal thickening in southern Tibet: insights from strongly fractionated ca. 43 Ma granites in the western Gangdese Batholith. *Lithos* **239**, 128–41.

Wang R, Richards JP, Hou ZQ, An F and Creaser RA (2015) Zircon U–Pb age and Sr–Nd–Hf–O isotope geochemistry of the Paleocene–Eocene igneous rocks in western Gangdese: evidence for the timing of Neo-Tethyan slab breakoff. *Lithos* **224–225**, 179–94.

Wang R, Tafti R, Hou ZQ, Shen ZC, Guo N, Evans NJ, Jeon H, Li QY and Li WK (2017) Across-arc geochemical variation in the Jurassic magmatic zone, Southern Tibet: implication for continental arc-related porphyry Cu-Au mineralization. *Chemical Geology* **451**, 116–34.

Wei YQ, Zhao ZD, Niu YL, Zhu DC, Liu D, Wang Q, Hou ZQ, Mo XX and Wei JC (2017) Geochronology and geochemistry of the Early Jurassic Yeba Formation volcanic rocks in southern Tibet: initiation of back-arc rifting and crustal accretion in the southern Lhasa Terrane. *Lithos* **278–281**, 477–90.

Wu CD, Zheng YC, Xu B and Hou ZQ (2018) The genetic relationship between JTA-like magmas and typical adakites: an example from the Late Cretaceous Nuri complex, southern Tibet. *Lithos* **320–321**, 265–79.

Wu FY, Yang YH, Xie LW, Yang JH and Xu P (2006) Hf isotopic compositions of the standard zircons and baddeleyites used in U–Pb geochronology. *Chemical Geology* **234**, 105–26.

Xia WJ, Yang ZS, Guan WQ and Zhang LY (2020) The petrogenesis of Amuxiong gabbro-granite complex in the middle segment of Gangdise belt. *Acta Petrologica et Mineralogica* **39**, 141–58 (in Chinese with English abstract).

Xiong XL, Liu XC, Zhu ZM, Li Y, Xiao WS, Song MS, Zhang S and Wu JH (2011) Adakitic rocks and destruction of the North China Craton: evidence from experimental petrology and geochemistry. *Science China Earth Sciences* **54**, 858–70.

Xu JF, Shinjo R, Defant MJ, Wang Q and Rapp RP (2002) Origin of Mesozoic adakitic intrusive rocks in the Ningzhen area of east China: partial melting of delaminated lower continental crust? *Geology* **30**, 1111–14.

Xu WC, Zhang HF, Luo BJ, Guo L and Yang H (2015) Adakite-like geochemical signature produced by amphibole-dominated fractionation of arc

magmas: an example from the Late Cretaceous magmatism in Gangdese belt, south Tibet. *Lithos* **232**, 197–210.

Yang ZM (2008) *The Qulong giant porphyry copper deposit in Tibet: magmatism and mineralization*. PhD thesis, Institute of Geology, Chinese Academy of Geological Sciences, Beijing. Published thesis.

Yin A and Harrison TM (2000) Geologic evolution of the Himalayan-Tibetan orogen. *Annual Review of Earth and Planetary Sciences* **28**, 211–80.

Yu F (2015) *The geochronology, geochemistry, petrogenesis of southern Yare pluton and its constrains for the metallogenic conditions of Miocene adakite-like porphyry in Lhasa Terrane*. PhD thesis, China University of Geosciences, Beijing. Published thesis.

Zeng LS, Gao LE, Xie KJ and Jing LZ (2011) Mid-Eocene high Sr/Y granites in the Northern Himalayan Gneiss Domes: melting thickened lower continental crust. *Earth and Planetary Science Letters* **303**, 251–66.

Zhang ZM, Zhao GC, Santosh M, Wang JL, Dong X and Shen K (2010) Late Cretaceous charnockite with adakitic affinities from the Gangdese batholith, southeastern Tibet: evidence for Neo-Tethyan mid-ocean ridge subduction? *Gondwana Research* **17**, 615–31.

Zhao W, Mechie J, Brown LD, Guo J, Haines S, Hearn T, Klemperer SL, Ma YS, Meissner R, Nelson KD, Ni JF, Pananont P, Rapine R, Ross A and Saul J (2001) Crustal structure of central Tibet as derived from project INDEPTH wide-angle seismic data. *Geophysical Journal International* **145**, 486–98.

Zhao XY, Yang ZS, Zheng YC, Liu YC, Tian SH and Fu Q (2015) Geology and genesis of the post-collisional porphyry–skarn deposit at Bangpu, Tibet. *Ore Geology Reviews* **70**, 486–509.

Zhao ZD, Mo XX, Dilek Y, Niu YL, DePaolo DJ, Robinson P, Zhu DC, Sun CG, Dong GC, Zhou S, Luo ZH and Hou ZQ (2009) Geochemical and Sr–Nd–Pb–O isotopic compositions of the post-collisional ultrapotassic magmatism in SW Tibet: petrogenesis and implications for India intra-continental subduction beneath southern Tibet. *Lithos* **113**, 190–212.

Zheng YC, Hou ZQ, Gong YL, Liang W, Sun QZ, Zhang S, Fu Q, Huang KX, Li QY and Li W (2014) Petrogenesis of Cretaceous adakite-like intrusions of the Gangdese Plutonic Belt, southern Tibet: implications for mid-ocean ridge subduction and crustal growth. *Lithos* **190**, 240–63.

Zheng YC, Hou ZQ, Li QY, Sun QZ, Liang W, Fu Q, Li W and Huang KX (2012a) Origin of Late Oligocene adakitic intrusives in the southeastern Lhasa terrane: evidence from in situ zircon U–Pb dating, Hf–O isotopes, and whole-rock geochemistry. *Lithos* **148**, 296–311.

Zheng YC, Hou ZQ, Li W, Liang W, Huang KX, Li QY, Sun QZ, Fu Q and Zhang S (2012b) Petrogenesis and geological implications of the Oligocene Chongmuda-Mingze adakite-like intrusions and their mafic enclaves, southern Tibet. *The Journal of Geology* **120**, 647–69.

Zheng YC, Liu SA, Wu CD, Griffin WL, Li ZQ, Xu B, Yang ZM, Hou ZQ and O'Reilly SY (2019) Cu isotopes reveal initial Cu enrichment in sources of giant porphyry deposits in a collisional setting. *Geology* **47**, 135–8.

Zheng YC, Wu CD, Tian SH, Hou ZQ, Fu Q and Zhu DC (2020) Magmatic and structural controls on the tonnage and metal associations of collision-related porphyry copper deposits in southern Tibet. *Ore Geology Reviews* **122**, 103509.

Zhou LM, Wang R, Hou ZQ, Li C, Zhao H, Li XW and Qu WJ (2018) Hot Paleocene-Eocene Gangdese arc: growth of continental crust in southern Tibet. *Gondwana Research* **62**, 178–97.

Zhu DC, Wang Q, Cawood PA, Zhao ZD and Mo XX (2017) Raising the Gangdese mountains in southern Tibet. *Journal of Geophysical Research: Solid Earth* **122**, 214–23.

Zhu DC, Wang Q, Chung SL, Cawood PA and Zhao ZD (2018) Gangdese magmatism in southern Tibet and India–Asia convergence since 120 Ma. *In Himalayan Tectonics: A Modern Synthesis* (ed. PJ Treloar), pp. 583–604. Geological Society of London, Special Publication no. 483.

Zhu DC, Wang Q, Zhao ZD, Chung SL, Cawood PA, Niu YL, Liu SA, Wu FY and Mo XX (2015) Magmatic record of India-Asia collision. *Scientific Reports* **5**, 14289.

Zhu DC, Zhao ZD, Niu YL, Mo XX, Chung SL, Hou ZQ, Wang LQ and Wu FY (2011) The Lhasa Terrane: record of a microcontinent and its histories of drift and growth. *Earth and Planetary Science Letters* **301**, 241–55.

Zhu DC, Zhao ZD, Pan GT, Lee HY, Kang ZQ, Liao ZL, Wang LQ, Li GM, Dong GC and Liu B (2009) Early Cretaceous subduction-related adakite-like rocks of the Gangdese Belt, southern Tibet: products of slab melting and subsequent melt–peridotite interaction? *Journal of Asian Earth Sciences* **34**, 298–309.